CONCEPT

Spectroscopic Techniques to Unravel Mechanistic Details in Light-Induced Transformations and Photoredox Catalysis

Simon De Kreijger,[a]† Martin Gillard,[a]† Benjamin Elias*[a] and Ludovic Troian-Gautier*[a],[b]

[a] S. De Keijger, Dr. M. Gillard, Prof. Dr. B. Elias, Prof. Dr. L. Troian-Gautier
Institut de la Matière Condensée et des Nanosciences (IMCN), Molecular Chemistry, Materials and Catalysis (MOST)
UCLouvain
Place Louis Pasteur 1 box L4.01.02, B-1348 Louvain-la-Neuve, Belgium

[b] Prof. Dr. L. Troian-Gautier
Wel Research Institute, Avenue Pasteur 6, 1300 Wavre, Belgium
E-mail: Benjamin.Elias@ulouvain.be, Ludovic.Troian@uclouvain.be

†These authors equally contributed to the manuscript.

Abstract: The rapid development of photo(redox) catalysis within the last decades is remarkable to the extent that the utilization of light-driven processes in organic chemistry has become a credible alternative to current thermal processes. Such advances offer tremendous opportunities of collaborations between scientific realms that can have a drastic impact on the development of the field. In this concept article, a special emphasis is placed on spectroscopic techniques that are used, or could be used, for light-induced transformations and photoredox catalysis applications. These include UV-VIS, IR and X-Ray transient absorption spectroscopy, laser pulsed radiolysis (PR), photo-induced chemically induced dynamic nuclear polarization (Photo-CIDNP), photoacoustic spectroscopy, time-resolved Raman spectroscopy (TRRS) and time-resolved dielectric loss spectroscopy (TRDL). The theoretical background behind each technique is briefly introduced followed by selected relevant examples from the literature.

1. Introduction

The use of light to drive chemical reactions has long been proposed as an alternative to our current classical use of fossil fuels. The sun represents one of the most abundant sources of renewable energy that can be harvested efficiently through chemical engineered solutions. For example, solar cells, first developed in 1954 by the Bell's laboratory,[1] that convert sunlight into electricity are now part of our daily landscape. Plants, that produce feedstock *via* photosynthesis, have inspired a plethora of scientists who have dedicated their research to the development of artificial photosynthetic systems.[2] The use of sunlight to mediate organic reaction had also been reported by Ciamician and Silber using prolonged exposure to sunlight.[3] More than a century later, the use of photosensitizers to initiate organic transformations using visible light is amongst the most prominent research area in photochemistry and organic chemistry. An outstanding amount of photosensitized chemical transformation have been reported, yet the reaction mechanism or the efforts to elucidate the mechanism have not always been as thoroughly investigated. This is now changing and to quote Vincenzo Balzani, Paola Ceroni et al. *"Elucidation of photochemical mechanisms in complex photocatalytic systems is difficult, but it is compulsory in order to make progress in the growing field of organic photocatalysis, which so far largely relied on empirical findings."*[4] In this concept article, we aim to provide the reader with recent reports on spectroscopic techniques that are used, or could be used, to investigate specific mechanistic aspects of photoredox catalysis. These techniques are briefly presented, alongside relevant examples from the literature.

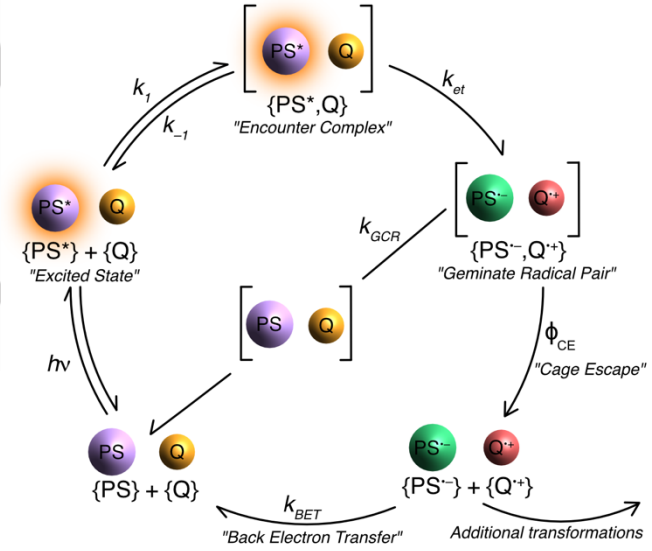

Figure 1. Photophysical and photochemical scheme describing the reaction between a photosensitizer (PS) and a quencher (Q) under light irradiation. The corresponding rate constant for electron transfer (k_{et}), geminate charge recombination (k_{GCR}) and back-electron transfer (k_{BET}) are indicated.

In a typical photophysical scheme for photoreactions depicted in **Figure 1**, photon absorption by a photosensitizer (PS) leads to the formation of an excited state (PS*) that can diffuse to form an encounter complex with a quencher (Q), from which an excited-state reaction could occur if the thermodynamics are favorable. The formation of an encounter complex is considered a prerequisite for bimolecular reactivity. The interaction between PS* and Q can be investigated through Stern-Volmer experiments, as developed by Otto Stern and Max Volmer in 1919.[5] To do so, the steady-state or time-resolved photoluminescence of the PS is recorded and monitored in the presence of increasing amounts of quencher. The ratio of the

steady-state photoluminescence (PLI_0) or the time-resolved photoluminescence (τ_0) without quencher and with known concentration of quencher (PLI or τ) is then plotted against the concentration of quencher. Different selected scenarios (amongst many) can then occur:

- Plots of PLI_0/PLI and τ_0/τ versus the concentration of quencher are linear and coincident. This observation is in line with a dynamic quenching mechanism (Eq.1), where PS and Q diffuse and undergo collisions during the quenching process. The slope, also known as the Stern-Volmer constant (K_{SV} in M^{-1}), gives access to the bimolecular quenching rate constant (k_q in $M^{-1}s^{-1}$), when divided by τ_0.

$$\frac{(PLI_0)}{(PLI)} = \frac{\tau_0}{\tau} = 1 + K_{SV}[Q] = 1 + k_q\tau_0[Q] \qquad \text{Eq.1}$$

- Plots of PLI_0/PLI are not linear and exhibit upward curvature. This is symptomatic of a static quenching mechanism, i.e. mostly when a non-emissive ground state adduct is formed. Information about this non-emissive adduct can sometimes be investigated by UV-Visible absorption changes during titrations, or by monitoring the initial amplitude (α) loss of the time-resolved photoluminescence.[6] Plots of α_0/α and PLI_0/PLI versus the concentration of quencher give information about the equilibrium constant, K_S, for quencher-chromophore adduct formation, Eq. 2**.** Note that this equation is only valid in cases where the ground-state adduct is completely non emissive and when the concentration of quencher is large in comparison to the concentration of the photosensitizer. The reader is directed toward an excellent tutorial review on static quenching for additional information.[7] Often, a combination of both processes, i.e., static and dynamic quenching takes place, and can be easily monitored using a combination of steady-state and time-resolved photoluminescence measurements. The dynamic process can be monitored by time-resolved photoluminescence measurements and Eq.1 whereas the upward curvature in a Stern−Volmer plot of PLI_0/PLI versus the concentration of quencher can be modelled using Eq. 3 which displays a quadratic dependence on the quencher concentration.

$$\frac{(PLI_0)}{(PLI)} = \frac{\alpha_0}{\alpha} = 1 + K_S[Q] \qquad \text{Eq. 2}$$

$$\frac{(PLI_0)}{(PLI)} = \frac{\alpha_0}{\alpha} \times \frac{\tau_0}{\tau} = 1 + (K_D + K_S)[Q] + K_D K_S[Q]^2 \qquad \text{Eq. 3}$$

Very importantly, whereas a decrease in photoluminescence indicates an excited-state quenching process, it does not inform on the exact nature of the quenching mechanism, i.e., electron and/or proton transfer, energy transfer, change in non-radiative rate constants, etc, which can only be investigated by more sophisticated techniques, as will be described in this concept article.

The pair of PS* and Q within the encounter complex can undergo electron transfer, a process perfectly explained with Marcus theory,[8] forming the geminate radical pair composed of either the oxidized PS ($PS^{\bullet+}$) and the reduced Q ($Q^{\bullet-}$) or the reduced PS ($PS^{\bullet-}$) and the oxidized Q ($Q^{\bullet+}$). This geminate radical pair can then undergo geminate charge recombination to form the initial PS and Q reactants or undergo cage escape (ϕ_{CE}) to generate the separated charged species. The solvent separated radicals can either undergo back-electron transfer (k_{BET}) or further react in catalytic transformations leading to the desired product formation. The investigation of these ϕ_{CE} processes for a given geminate radical pair is of great interest as the efficient formation of the solvents separated radicals is a key parameter to control the optimization of photocatalytic reaction.[9] If the cage-escape yields are null, the geminate radical pair undergoes in-cage geminate charge recombination to form the ground-state product and the formation of charge-separated product will not be observed experimentally.

These cage-escape yields are often measured by comparative actinometry techniques using equations 4 and 5. To do so, the absorption changes generated from the oxidized PS ($PS^{\bullet+}$) or reduced PS ($PS^{\bullet-}$) are compared with the absorption changes of the excited state of a reference actinometer (ES_{ref}) and normalized by their relative absorptances at the excitation wavelength (λ_{exc}). The change in molar absorption coefficient ($\Delta\varepsilon$) for the actinometer are known from the literature in some cases or can be determined by variable power excitation measurements using transient absorption measurements, whereas the $\Delta\varepsilon$ values of the oxidized or reduced photosensitizers can be determined by photolysis,[10] spectroelectrochemistry[11] or using transient absorption spectroscopy with reference electron acceptor/donors.[12] It is best to measure the changes in absorption following pulsed light excitation at wavelengths where the $\Delta\varepsilon$ between the ground and reduced or oxidized state is maximized.[9aj]

$$\Phi_{CE} = \frac{\Phi}{\%\ PL\ Quenched} \qquad \text{Eq. 4}$$

$$\Phi = \left(\frac{\frac{\Delta A_{PS^-}}{\Delta\varepsilon_{PS^-}}}{\frac{\Delta A_{ES_{ref}}}{\Delta\varepsilon_{ES_{ref}}}}\right)\left(\frac{1-10^{-Abs_{ref}(\lambda_{exc})}}{1-10^{-Abs_{PS}(\lambda_{exc})}}\right) \qquad \text{Eq. 5}$$

Final ϕ_{CE} values are obtained by comparing the relative yield of $PS^{\bullet+}$ or $PS^{\bullet-}$ produced (ϕ) to the percentage of quenched photoluminescence (%PL), determined *via* time-resolved or steady-state PL measurements. A linear regression of all the data point by constraining the Y-intercept at 0 provides a slope that corresponds to the cage-escape yield value.[9b, 13]

In sum, **Figure 1** represents a generally accepted model that describes light induced reactions that serves as a basis to our understanding of fundamental aspects that govern excited-state reactivity. As mentioned earlier, the approach developed by Otto Stern and Max Volmer is considered a robust approach to investigate the first step of excited-state reactivity. Yet, it does not provide in-depth mechanistic information. For that, more detailed spectroscopic experiments are needed, which are presented in this concept article, in hope to inspire the growing community of researcher and favor the collaborations between disciplines that will undoubtedly lead to significant advances in the field.

Simon De Kreijger is a Ph.D. student and teaching assistant at the Institute of Condensed Matter and Nanosciences, Université catholique de Louvain (UCLouvain). He undertook a 4-months internship in materials chemistry at the University of Cambridge (2017) in the laboratory of Pr. A. E. H. Wheatley. He then completed his Master thesis (2018) under the supervision of Pr. B. Elias in the field of solar energy conversion. His research is mainly focused on the development and tuning of photosensitizers properties for hydrogen photoproduction or halide oxidation.

Martin Gillard received his Ph.D. in chemistry in 2023 from Université catholique de Louvain (UCLouvain). He completed a 4-month training in total synthesis and methodology in the laboratory of Pr. J. W. Burton at the University of Oxford in 2016. He then undertook his Master thesis and his Ph.D. thesis in photochemistry in the laboratory of Pr. B. Elias at UCLouvain as a teaching assistant. His Ph.D. thesis focused on the design and study of new metal complexes towards anticancer theranostic applications. He's currently a postdoctoral researcher and teaching assistant at UCLouvain.

Benjamin Elias obtained his Ph.D. in chemical science from the Université libre de Bruxelles (ULB) in 2005. After a post-doctoral research stay in the group of Prof. J. K. Barton (California Institute of Technology) where he worked on the use of transition metal complexes to unravel DNA-mediated positive and negative charge transport processes, he was appointed associated professor (2008), professor (2016) and full professor (2022) at UCLouvain. His research group works on the development of new photochemotherapeutic agents and photo-active compounds for light induced transformations. He is currently the vice-dean of the Faculty of Science.

Ludovic Troian-Gautier received his Ph.D. in chemistry (2014) from the Université libre de Bruxelles (ULB). He then worked at a spin-off focusing on surface modification using calix[4]arene derivatives. Between 2015 and 2019, he performed research within the Alliance for Molecular PhotoElectrode Design for Solar Fuels directed by Prof. G. J. Meyer at UNC-Chapel Hill. In May 2019, he started a Chargé de Recherches position (F.R.S.-FNRS) at ULB and, in October 2022, he was promoted to Chercheur Qualifié F.R.S.-FNRS at UCLouvain where he pursues his research endeavors on mechanistic photoredox catalysis and energy related challenges.

2. Spectroelectrochemistry

2.1. Technique overview

Spectroelectrochemistry (SEC) combines advantages of both electrochemistry and steady-state spectroscopy to provide simultaneous characterization of redox potentials and the corresponding spectroscopic signatures of the oxidized or reduced species. This approach can be combined to several spectroscopic techniques (UV-vis, NIR, IR, Raman, EPR,…) although most examples are reported using UV-Vis and NIR spectroscopy. [9e, y, 13-14] SEC is often used as one of the first step in mechanistic investigations as it can be performed on photosensitizers or reactants in solution or anchored at the surface of photoelectrodes. SEC can therefore provide essential information on the spectroscopic properties of reaction intermediates produced during photoredox catalysis. For example, SEC can be used to determine the absorption spectra and the corresponding molar absorption coefficient of any reduced or oxidized species (photocatalyst/electron donor/reagents) that could be formed during the reaction, as long as they are electrochemically stable. These spectra can then be correlated to transient absorption data to determine the nature of key intermediates involved in a photoredox catalytic process. SEC is therefore a powerful technique for understanding and identifying the species involved in light-induced reaction mechanism.

2.2. Selected examples from the literature

Spectroelectrochemistry was used, amongst others, by Meyer and co-workers who reported a sensitized material prepared by a layer-by-layer assembly approach to spatially arrange redox active species and photosensitizers on a conductive indium-doped tin oxide thin film.[14i, k] This assembly consisted of a methyl viologen electron acceptor, a phosphonate $[Ru(bpy)_3]^{2+}$ analogue as photosensitizer, a phosphonate $[Fe(tpy)_2]^{2+}$ derivative as primary electron donor and either a triphenylamine derivative as secondary electron donor or a ruthenium water oxidation catalyst (WOC) (**Figure 2**).[14i, k] Spectroelectrochemistry was used to determine the redox potential of each species anchored on the indium-doped tin oxide this film as well as the changes in UV-Visible absorption occurring upon changes in redox state. Nernst equation was used to analyse the absorption values taken during stepwise application of increasingly positive potentials (**Figure 2**). Reductive spectroelectrochemistry of nITO |-MV provided the one electron reduction potential of the methylviologen acceptor, $E^0(MV^{2+/+\bullet}) = -0.42$ V vs NHE. Oxidative electrochemistry allowed to determine the formal reduction potentials (**Figure 2A**) for the other species, with $E^0(TPA^{+/0}) = 1.10$ V vs NHE, $E^0(Fe^{III/II}) = 1.13$ V vs NHE (**Figure 2B**), and $E^0(S^{+/0}) = 1.35$ V vs NHE (**Figure 2C**).[14i, k] The different oxidation states of the water oxidation catalyst and the associated UV-Vis spectra were also determined through this technique.[14k] The determination of these formal potential allowed the authors to understand the thermodynamic associated with the photoelectrode assembly and understand the nanosecond transient absorption experiments, not detailed in this

section. In conclusion, spectroelectrochemistry is a versatile technique that allows to characterize photosensitizers and reagents both in terms of redox potential and spectroscopic features. It provides the experimentalist with thermodynamic parameters and spectroscopic features that can help rationalize reaction mechanisms and corroborate spectral features obtained with other spectroscopic techniques (*vide infra*).

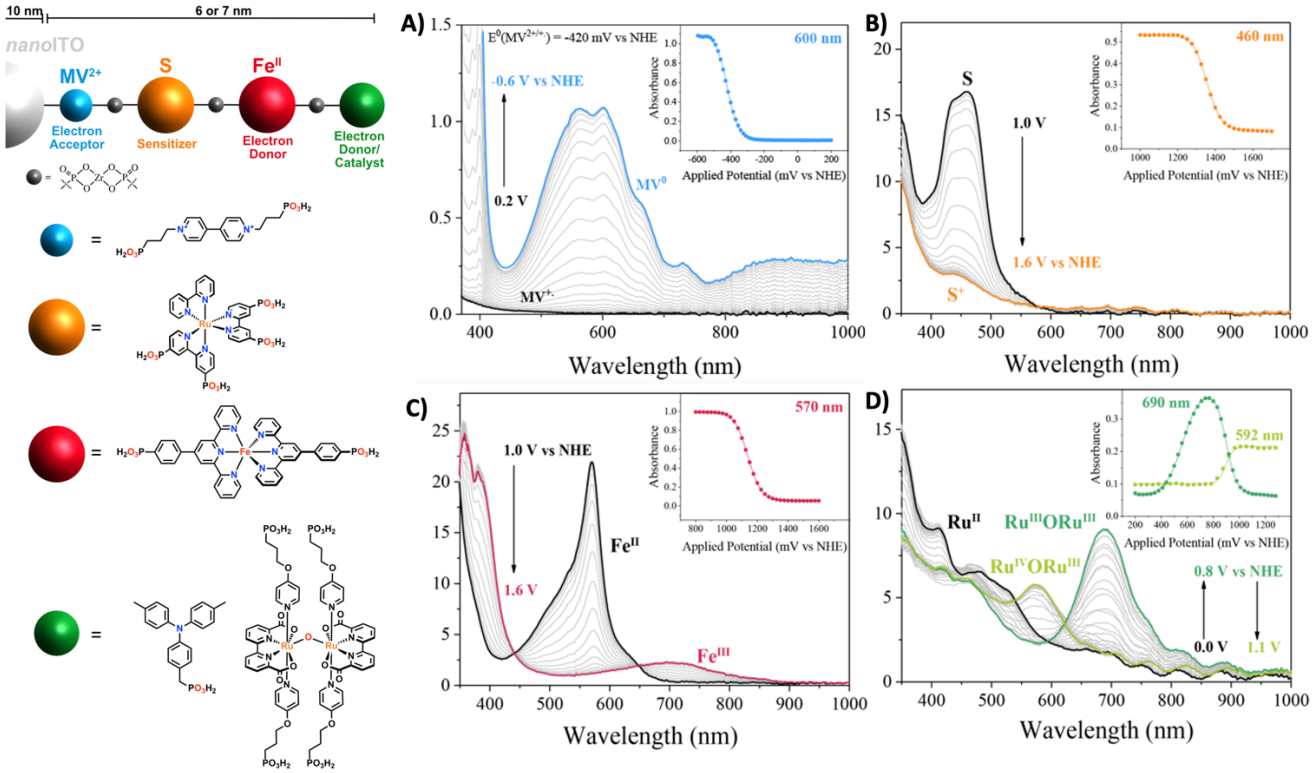

Figure 2. Absorption spectra measured during electrolysis of the individual components within the assembly nanoITO|-MV^{2+}-S-Fe^{II}-Ru^{II} (left) with: A) Absorption spectra measured during the reduction of nanoITO|-MV^{2+}, B) Absorption spectra measured during the oxidation of nanoITO|-S, C) Absorption spectra measured during the oxidation of nanoITO|-Fe^{II}, and D) Absorption spectra measured during the oxidation of nanoITO|-WOC. The insets show absorbances at key wavelengths as a function of applied potential for the oxidation to $Ru^{III}ORu^{III}$ and $Ru^{IV}ORu^{III}$ (data in green), with the latter absorbing at 560 nm. The corresponding reduction potentials were obtained using a modified Nernst equation.[15] All measurements were performed in 0.1 M acetate buffer (pH 4.65) with 0.5 M $NaClO_4$ as the supporting electrolyte. Adapted with permission from reference.[14k] Copyright 2019 American Chemical Society.

3. UV-Visible Transient Absorption Spectroscopy

3.1. Technique overview

UV-Visible transient absorption spectroscopy probably represents the most prominent technique to study reaction intermediates and unravel important mechanistic details. It is part of the pump-probe techniques, in which a sample is illuminated with a laser pulse (the pump) leading to the formation of an excited state. An analytical lamp (the probe) then records an absorption spectrum as a function of time, usually from the fs up to seconds time range, depending on the apparatus. The absorption signal is then compared to a signal without laser illumination and a difference spectrum allows to obtain the changes in absorption before and after pulsed light irradiation.[16] This technique provides UV-Visible absorption spectra of the excited state and, central to this perspective, the UV-Visible absorption spectra of key intermediates if the excited photosensitizer reacts with a quencher. If the UV-Visible absorption spectra of the oxidized and reduced species are known, it is also possible to determine the nature of the operative quenching mechanism, *i.e.,* whether the light-induced reaction proceeds *via* oxidative or reductive quenching or *via* energy transfer. As mentioned in the introduction, charge-separated products will only be observed if the cage-escape yields are non-null.

The direct observation of photoproducts and their evolution in time is a clear advantage of UV-Visible nanosecond transient absorption spectroscopy. Even more importantly, if the formation or consumption of products/reactants can be monitored at specific wavelengths, it is possible to gain access to the kinetic rate constants for any given process. Single wavelength absorption changes can be fit to obtain the corresponding observed rate at a given concentration. By plotting the observed rates obtained at different concentration as a function of quencher concentration, one can obtain the corresponding kinetic rate constants.

A typical transient absorption set-up is composed of two main components (**Figure 3**). An excitation part that contains the excitation laser and the optics required to convey light to the sample and a detection unit composed of a light source that probes the sample and is collected by a detector. The wavelength of the excitation laser can be tuned to finely excite the system of interest, while the light probe is usually a broad-band spectrum source. While transient absorption probing is commonly performed by UV-Visible light, other region of the electromagnetic

spectrum can be used including infrared radiation and X-rays (*vide infra*).

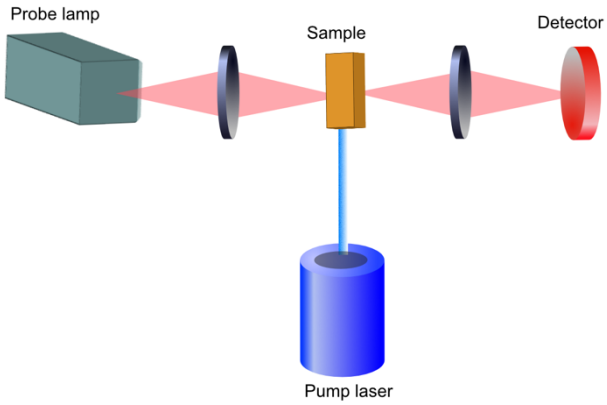

Figure 3. General representation of a transient absorption experimental set-up.

3.2. Selected examples from the literature

Ru(II) polypyridyl complexes probably represents the most studiedcategory of photosensitizers for application in excited-state electron transfer chemistry, although there are currently tremendous research endeavors by pioneering groups that develop earth abundant photosensitizers for such applications.[9y, 14f, 17] Nevertheless, Ru(II) photosensitizers are very useful to introduced the concept of transient absorption spectroscopy as these photosensitizers present metal-to-ligand charge transfer (MLCT) excited-state, where the Ru(II) center is formally oxidized to Ru(III) and one of the ancillary ligand is formally reduced.[18] This creates a "loss" in the typical ground state absorption, which is characterized by a bleach of the MLCT transition when recording a transient absorption spectrum (**Figure 4**). The reduced ligand is responsible for novel transitions compared to the ground state, which leads to positive absorption features in the transient absorption spectra. These positive and bleached signals imply the presence of isoabsorptive points, *i.e.,* points where the absorbance of the ground state and the excited state remains unchanged. In the difference spectra, this corresponds to ΔAbs = 0 (**Figure 4**). Most often, the corresponding reduced or oxidized species absorbs at these ground and excited-state isosbestic points which enables to study the formation of these species without contribution from the excited-state (**Figure 4**). This facilitates the determination of rate constants for the formation of various products.

For most photosensitizers exhibiting MLCT excited states, the presence of isosbestic points is often observed and facilitates the determination of the rate constants. In Ir(III) PS, the excited state is often composed of a manifold of different transitions which, in most cases, leads to only positive ΔAbs features in transient absorption spectroscopy.[19] This obviously complicates the determination or the corresponding rate constants as the signal of the oxidized or reduced species will be superimposed with the signal from the excited state. It is however possible to extrapolate the corresponding rate constant by recording excited-state lifetimes and using that value in the corresponding fit. Most of the time, researchers use transient absorption spectroscopy to confirm the operative quenching mechanism and to determine the associated kinetic rate constant for selected processes (forward electron transfer, back-electron transfer, hydrogen atom transfer, …).

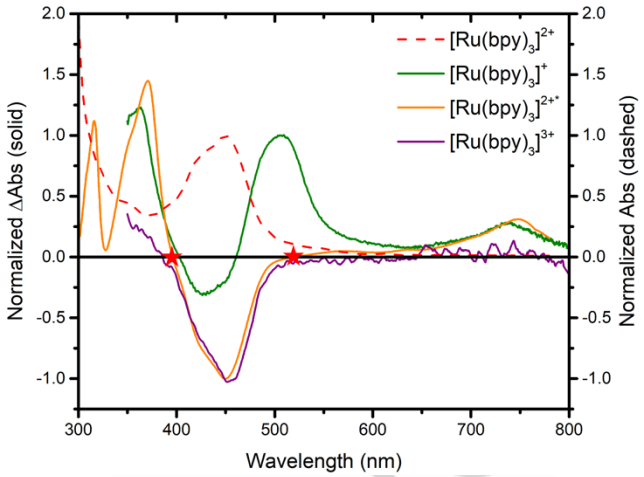

Figure 4. Ground-state (dashed), excited-state (orange), oxidized (purple) and reduced (green) spectra of $[Ru(bpy)_3]^{2+}$. The transient absorption spectrum of the reduced species was recorded using sodium ascorbate whereas the spectrum of the oxidized species was recorded using sodium persulfate. Experiments were carried out in argon purged MilliQ water. The spectra were recorded 200 ns after pulsed 420 nm light excitation. Red stars indicate the ground-to-excite-state isosbestic points. Experiments were carried out for this concept article.

A great series of examples that highlights the vibrancy of the field of photoredox catalysis can be found in the sensitization-initiated electron transfer story. In 2017, König and co-workers developed a photoredox catalytic system based on sensitization-initiated electron transfer to combine the absorption and redox potentials properties of two distinct molecules through a bimolecular energy transfer process.[20] The reaction was optimized with 2-bromobenzonitrile (model substrate), $[Ru(bpy)_3]^{2+}$ (photosensitizer), pyrene (Pyr, energy acceptor and redox active molecule), *N*-methylpyrrole (radical trapping agent) and *N*,*N*-diisopropylethylamine (DIPEA, sacrificial electron donor). At the time, the proposed catalytic cycle for this C–H arylation reaction followed the following steps: 1) Excitation of $[Ru(bpy)_3]^{2+}$ to reach the corresponding $[Ru(bpy)_3]^{2+*}$ excited state, 2) Triplet-triplet energy transfer from $[Ru(bpy)_3]^{2+*}$ to Pyr to form the corresponding triplet Pyr(T_1), 3) Reductive quenching of Pyr(T_1) by DIPEA to generate $Pyr^{\bullet-}$ and $DIPEA^{\bullet+}$, 4) Electron transfer from $Pyr^{\bullet-}$ to the aryl halide to generate the aryl halide radical precursor and regenerating Pyr, 5) Fragmentation of the aryl halide radical to yield the aryl radical, which reacts with the trapping agent to yield the C–C coupling product.

In a correspondence paper, Balzani, Ceroni and co-workers questioned the feasibility of the proposed electron transfer from DIPEA to the Pyr(T_1).[4] Based on thermodynamic considerations, it was estimated that the electron transfer from DIPEA to the Pyr(T_1) was uphill by ~1eV and therefore seemed very unlikely. An alternative thermodynamically allowed mechanism was then proposed. The latter involved energy transfer from the photoexcited $[Ru(bpy)_3]^{2+}$ to Pyr followed by triplet-triplet annihilation of two Pyr(T_1) species to yield a Pyr(S_1) intermediate that was quenched by reductive electron transfer from DIPEA.

In their reply, König and co-workers proposed another alternative exergonic reaction pathway involving the formation of $[Ru(bpy)_3]^+$ by reductive quenching of photoexcited $[Ru(bpy)_3]^{2+}$ by DIPEA. This reaction is slightly uphill and kinetically slow but such sacrificial amine derivatives are known to reduce $[Ru(bpy)_3]^{2+}$ under irradiation, which allows to accumulate $[Ru(bpy)_3]^+$. With a reduction potential of –1.33 V vs SCE,[18, 21] $[Ru(bpy)_3]^+$ could reduce Pyr(T_1) formed by the previously mentioned triplet-triplet energy transfer, yielding the $Pyr^{\bullet-}$ key intermediate.[22]

In 2020, Moore and co-workers investigated the different proposed mechanistic pathways for this reaction using nanosecond transient absorption spectroscopy.[9ad] Excited-state quenching of $[Ru(bpy)_3]^{2+*}$ was observed when increased concentrations of pyrene were added. This enable the determination of the bimolecular quenching rate constant for triplet-triplet energy transfer as k_{TTET} = 3.09 x 10^8 M^{-1} s^{-1}. Clear appearance of excited-state absorption features at 420 and 520 nm were in line with the formation of Pyr(T_1). Interestingly, a decrease in the Pyr(T_1) was observed upon increasing the initial Pyr concentration, pointing towards the presence of a triplet-triplet annihilation process which was confirmed by fluorescence lifetime measurements at 390nm (Pyr(S_1) fluorescence). The excited-state quenching of $[Ru(bpy)_3]^{2+*}$ was also investigated with DIPEA which allowed to determine the corresponding electron transfer rate constant, k_{et} = 1.31 x 10^7 M^{-1} s^{-1}. Formation of the corresponding reduced $[Ru(bpy)_3]^+$ complex was confirmed by transient absorption spectroscopy. Finally, the photocatalytic system was investigated in the presence of varying concentrations of both Pyr and DIPEA. The lifetime of Pyr(T_1) and $[Ru(bpy)_3]^+$ was monitored at different concentrations. A clear decrease in the lifetime of $[Ru(bpy)_3]^+$ with increasing concentration of Pyr was identified. Furthermore, the Pyr(T_1) lifetime was quenched as a function of the initial DIPEA concentration. As the reaction of photoexcited $[Ru(bpy)_3]^{2+}$ with DIPEA resulted in the formation of $[Ru(bpy)_3]^+$, these transient absorption results were consistent with the formation of the $Pyr^{\bullet-}$ through an electron transfer event form $[Ru(bpy)_3]^+$ to Pyr(T_1). The possibility of a triplet-triplet annihilation pathway for the $Pyr^{\bullet-}$ generation was investigated by TCSPC lifetime measurements using $[Ru(bpy)_3]^{2+}$ in the presence of both Pyr and DIPEA. Formation of Pyr(S_1) by triplet-triplet annihilation was also observed. However, the intensity of Pyr(S_1) was reduced to less than 5%. Further calculations and control experiments revealed that the majority of the Pyr(T_1) is consumed by electron transfer with $[Ru(bpy)_3]^+$ while only minor proportion (<5%) undergoes triplet-triplet energy transfer to form Pyr(S_1) or other non-radiative processes. Taken together, these results allowed to unravel the reaction mechanism depicted in **Figure 5**.

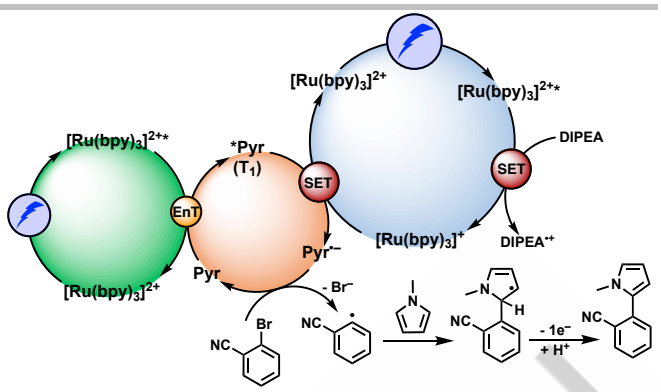

Figure 5. Proposed sensitization-initiated electron transfer mechanism showing the formation of both Pyr(T_1) and $[Ru(bpy)_3]^+$ by visible light absorption, and subsequent formation of $Pyr^{\bullet-}$ proposed by Moore and co-workers.[9ad] SET stands for "single electron transfer" and EnT stands for "energy transfer".

Recently, Swierk and co-workers reported a complete mechanistic investigation of a photoinduced α-aminoarylation reaction by combining steady-state photochemical and transient absorption spectroscopy. 1,4-dicyanobenzene (DCB) was coupled to *N*-phenylpyrrolidine (NPP) to generate 4-(1-phenyl-2-pyrrolidinyl)benzonitrile using $[Ir(ppy)_3]$ as the photosensitizer and NaOAc as a base.[23] The electron transfer step between DCB and $[Ir(ppy)_3]$ was firstly investigated by Stern-Volmer analysis which yielded a quenching rate constant k_q = 2.2 x 10^9 M^{-1} s^{-1}. Using transient absorption spectroscopy, the initial spectra (100 ns after laser pulse) presented positive features at wavelengths longer than 460 nm and a bleach centered at 380 nm that were assigned to the formation of Ir(IV). Another new positive absorption at 430 nm was this time attributed to $DCB^{\bullet-}$. At time scale longer than 1 μs, changes in the transient spectra (new absorption at 860 nm, bleach at 380 nm and a blue shift of the absorption feature at 600 nm) were pointing toward the formation of a new species. This was ascribed to the formation of a DCB dimer formulated as $(DCB)_2^{\bullet-}$ and confirmed by spectroelectrochemistry at high concentration of DCB.

A kinetic model was developed to understand the reaction between $[Ir(ppy)_3]$, DCB and $(DCB)_2^{\bullet-}$. This model included several steps, such as the back electron transfer between Ir(IV) and $DCB^{\bullet-}$ (k_{recomb}), pairing of DCB and $DCB^{\bullet-}$ (k_{pair}), and electron transfer between Ir(IV) and $(DCB)_2^{\bullet-}$ ($k_{recomb2}$). This model was then used to fit the single wavelength absorption changes recorded at characteristic wavelengths. A recombination rate constant, k_{recomb} = 5.4 x 10^9 M^{-1} s^{-1}, was calculated and points towards a diffusion-controlled process. Nevertheless, given the low concentration of Ir(IV) and $DCB^{\bullet-}$, it was proposed that the preponderant pathways was the reaction between $DCB^{\bullet-}$ and excess DCB to form $(DCB)_2^{\bullet-}$ with a rate constant of 1.1 x 10^6 $M^{-1}s^{-1}$. Back electron transfer then took place between Ir(IV) and $(DCB)_2^{\bullet-}$ with $k_{recomb2}$ = 6.0 x 10^9 $M^{-1}s^{-1}$.

NPP was then added to the reaction mixture. On short time scale the transient spectra were completely different with a broad absorption from 400-600 nm with a sharp peak at 440 nm as well as a slight increase in the near-IR region. The broad 400-600 nm absorption was assigned to the formation of $NPP^{\bullet+}$ and the peak at 440 nm to $DCB^{\bullet-}$. No features could be ascribed to the Ir photosensitizer, which suggest that oxidation of NPP is completed

within 100 ns. A minimum value of k_{ox} of 4 x 10^8 $M^{-1}s^{-1}$ was then determined using a kinetic modelling. After 10 μs, drastic changes in the transient absorption spectra were observed which agreed with the formation of an alkane radical.[24]

Single wavelengths absorption changes confirmed the formation of a new species on a 10-100 μs timescale which decayed on the millisecond timescale. Here again, the kinetic model developed in their study was further developed to include the deprotonation of $NPP^{\bullet+}$ (k_{deprot}) and the coupling of $NPP^{\bullet}$ and $(DCB)_2^{\bullet-}$ (k_{couple}). Unproductive pathways, such as the electron transfer between $NPP^{\bullet+}$ and $DCB^{\bullet-}$ ($k_{rad\ recomb}$) and $(DCB)_2^{\bullet-}$ were also considered to gain a complete mechanistic view of this photoactivated α-aminoarylation reaction (**Figure 6**). It should be emphasized that the determination of kinetic rate constant requires these experiments to be carried out at several concentrations of individual reactants.

Besides electron transfer, photocatalytic processes can also occur *via* energy transfer mechanisms. For energy transfer, two very different interactions can be involved. Both electron exchange (orbitals overlap – Dexter type) and dipole-dipole interactions (dipole fields overlap – Förster type) may offer access to an excited state active species through photosensitization from photo-excited chromophores. While electrons transfer requires a thermodynamic match between the redox potential of the donor and the acceptor, the energy transfer process efficiency mostly depends on optimization of spectral or molecular orbital overlap, according to the associated energy transfer mechanism, i.e. Förster or Dexter energy transfer.[25]

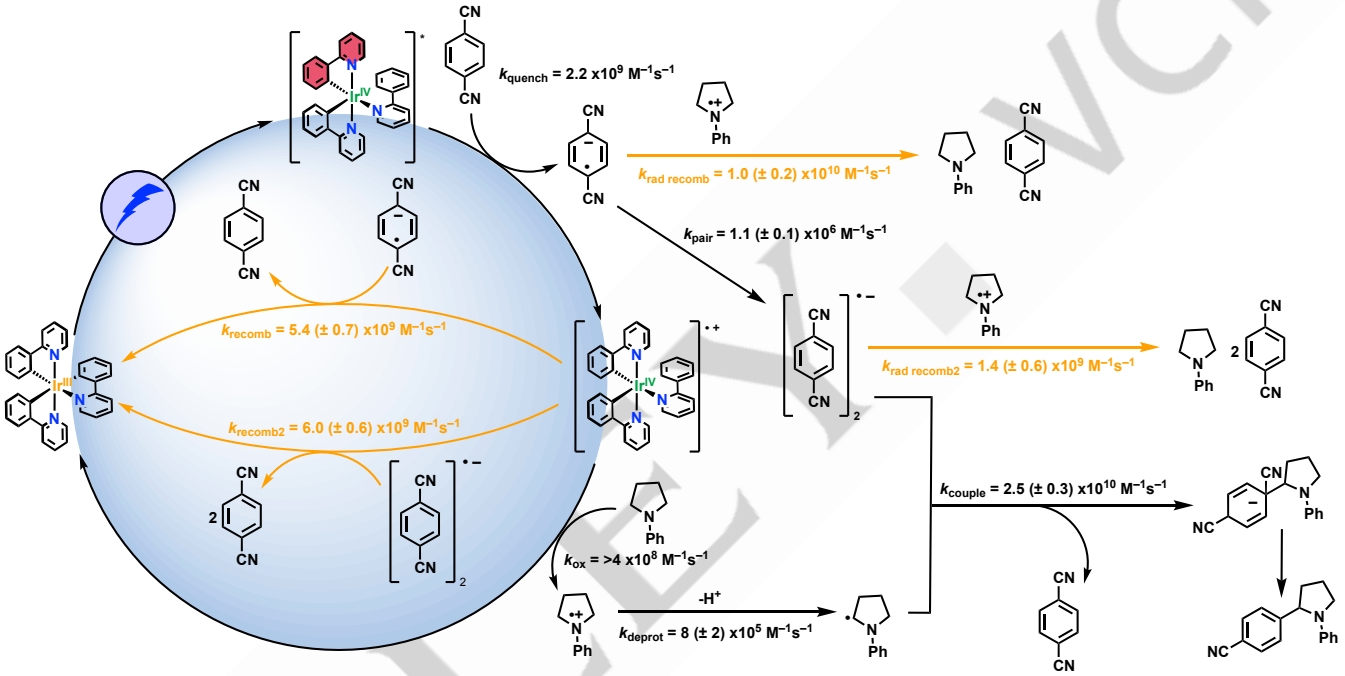

Figure 6. Mechanism for the α-aminoarylation reaction between N-phenylpyrrolidine (NPP) and 1,4-dicyanobenzene (DCB) as proposed by Swierk and co-workers.[23] Catalytically unproductive pathways are represented with orange arrows.

In this context, MacMillan and co-workers reported the coupling of carboxylic acid with aryl halide to form *O*-aryl ester products using a dtbbpy-Ni(0) complex as the coupling catalyst, [Ir(ppy)$_3$] as the photosensitizer and tert-butyl-isopropylamine as the base. The proposed catalytic cycle started with the oxidative addition of aryl halide to the Ni(0) complex to generate a Ni(II)(aryl) species that could rapidly coordinate a carboxylate nucleophile to yield a Ni(II)(aryl) carboxylate species. At this stage, a triplet-triplet energy transfer step from the excited photosensitizer to the Ni(II) species was proposed to induce the reductive elimination and generate the *O*-aryl ester product. This energy transfer mechanism was supported by the correlation between the catalytic reaction yield and the triplet energy of Ir(III) complexes and an anticorrelation with the oxidizing power of different Ir(III) based photocatalyst.[26]. In order to confirm that the reductive elimination step was induced by triplet-triplet energy transfer, Scholes and co-workers deciphered the mechanism of an iridium/nickel-catalyzed C–O cross-coupling reaction from time-resolved spectroscopic and transient absorption studies.[27] Time-resolved Stern-Volmer quenching experiment between [Ir(ppy)$_3$] and a Ni(II)(Ar) acetate complex yielded a quenching rate constant k_q = 1.77 x10^9 $M^{-1}s^{-1}$. The mechanism of excited-state quenching was then studied by transient absorption spectroscopy as both photoinduced electron transfer and energy transfer could be operative. On the one hand, electron transfer would lead to the formation of the corresponding Ir(IV)/Ni(I) (oxidative electron transfer) or Ir(II)/Ni(III) (reductive electron transfer) species. On the other hand, energy transfer would lead to the ground-state Ir(III) photosensitizer and the formation of the photoexcited Ni(II) catalyst. Pulsed light excitation at 400 nm led to the concomitant formation of excited Ir and Ni species due to their overlapping absorption features. The short excited-state lifetime of the Ni complex (τ = 4.22 ns) did not lead to any quenching processes. Absorption changes corresponding to [Ir(ppy)$_3$]* (ground-state bleach at 410 nm and absorbance at 520 nm) were recorded at timescale longer than the decay of the excited Ni complex.

Excited state population dynamics showed that $[Ir(ppy)_3]^*$ decayed to the ground state on the microsecond time scale (**Figure 7**). The quenching rate constant, k_q = 1.70 x10^9 M^{-1} s^{-1}, for the excited-state energy transfer from $[Ir(ppy)_3]^*$ to Ni(II)(Ar) acetate was then extracted from decay data using different concentrations of Ni(II)(Ar) acetate. This value is consistent with the one determined by classical time-resolved Stern-Volmer analysis. The role of tert-butyl-isopropylamine base used in the reaction was also assessed due to its potential role as hole-electron transfer relay between $[Ir(ppy)_3]^*$ and the Ni(II)(Ar) acetate. To investigate this possibility, transient absorption spectroscopy was performed in the presence of the three components and minimal changes were observed for the lifetime of $[Ir(ppy)_3]$ compared to the mixture without the amine, pointing towards the dominant role of Ni(II)(Ar) acetate reacting with the Ir(III) excited state (**Figure 7**). The proposed reaction mechanism implies then that energy transfer occurs from $[Ir(ppy)_3]^*$ and generates the ground-state $[Ir(ppy)_3]$, concomitantly producing a spectroscopically silent triplet excited state of Ni(II) accounting for the correlated lifetime decay and the lack of new signals.

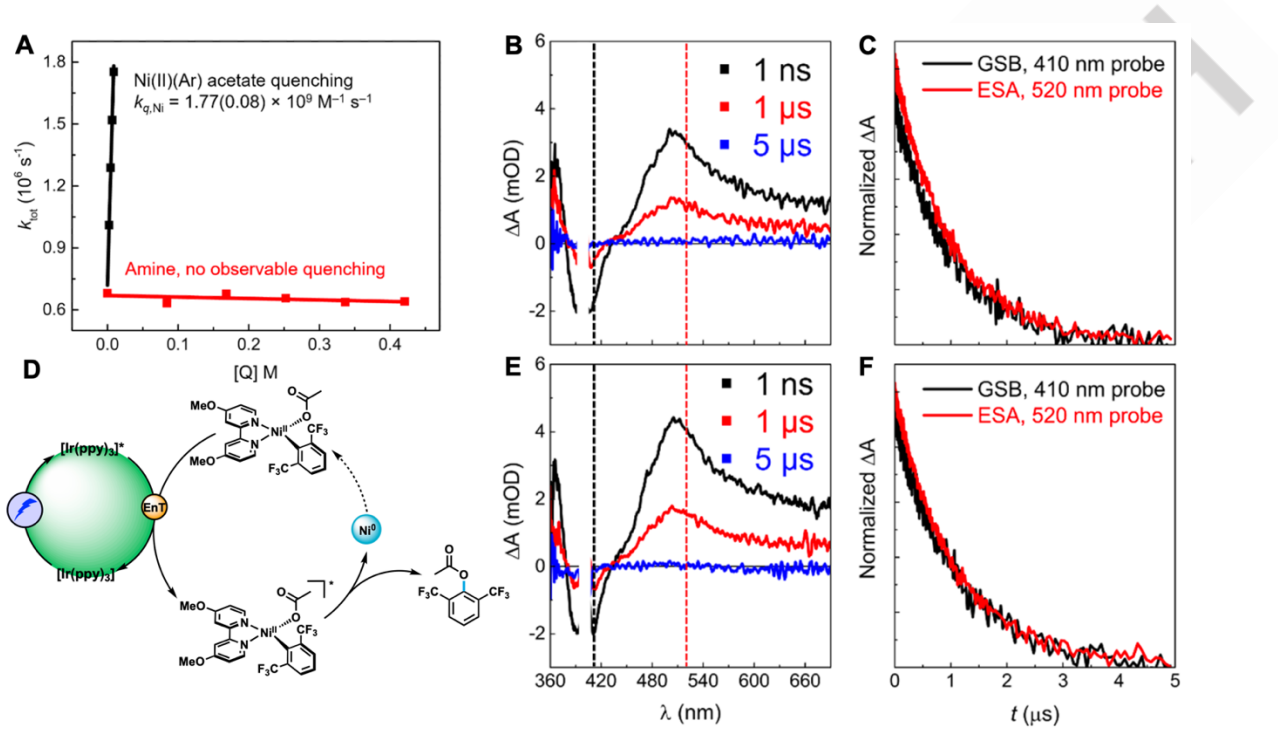

Figure 7. (a) Stern-Volmer plot for the quenching of $[Ir(ppy)_3]^*$ by Ni(II)(Ar) acetate (black) and *tert*-butyl-isopropyl amine (red). (b) Temporal evolution of photoinduced dynamics of a mixture of the $[Ir(ppy)_3]$ and Ni(II)(Ar) acetate in DMF, λ_{exc} = 400 nm. (c) Single-wavelength traces of the corresponding mixtures in (b) at 410 nm (t = 0.93(0.02) μs) and 520 nm (t = 1.00(0.01) μs). (d) Proposed mechanism for the C–O cross-coupling reaction. (e) Temporal evolution of photoinduced dynamics of a mixture of $[Ir(ppy)_3]$, Ni(II)(Ar) acetate and *tert*-butyl-isopropyl amine in DMF, λ_{exc} = 400 nm. (f) Single-wavelength traces of the corresponding mixture in (e) at 410 nm (t = 0.94(0.04) μs) and 520 nm (t = 1.03(0.01) μs). Adapted with permission from reference[27]. Copyright 2020 American Chemical Society.

Recently, a Fe(III) photosensitizer, $[Fe(phtmeimb)_2]^+$, first reported by Wärnmark et al., was used to perform visible light dehalogenation reaction of 4-bromobenzyl 2-chloro-2-phenylacetate.[9b] As this example gathers the use of several spectroscopic techniques, we sought to develop it throughout this concept article. The green-light induced dehalogenation reaction was shown to operate efficiently in dichloromethane, but the dehalogenation yields dropped significantly when acetonitrile or DMF were used. It was shown by nanosecond transient absorption spectroscopy that this drop in yield was due to a significant drop in cage-escape yields. Indeed, cage escape yields measured by comparative actinometry in DMF and CH_3CN were less than 7% but reached higher values (between 36% and 63% depending on the quencher) in CH_2Cl_2. This difference in the formation of separated charged species was observed despite the very similar excited-state quenching rate constants in all three solvents.[9b] These results were in line with the low cage escape yield (5%) reported by Wärnmark et al. for both *N*-phenylamine electron donor and methyl-viologen electron acceptor in CH_3CN.[9y] They were also consistent with those reported by Persson *et al.*, in which electron transfer between DMA and PS* only resulted in observable photoproducts at very large DMA concentration (>500 mM), attributed to ultrafast spin-allowed geminate charge recombination between the reduced PS and oxidized DMA (~ 0.2 ps).[9z]

UV-Visible transient absorption spectroscopy for photoredox catalysis application is most often performed on the nanosecond to second timescale as these processes often rely on diffusion processes. It is however also possible to perform similar transient absorption measurements on the femtosecond timescale. This allows the investigation of ultrafast photoinduced processes occurring in the excited electronic states. Information on elementary processes such as solvation, chemical reaction, conformational change, excitonic energy or electron transfer in solution can also be probed by this powerful technique. The measurement consists in a series of differential spectra spanning time delays from several femtoseconds to a few nanoseconds after the trigger by the visible-light pump.[28]

In the case of the Fe(III) photosensitizer, femtosecond transient absorption was used to confirm that the use of CH_2Cl_2 led to large photoproducts yields and to a decrease in the rate constant for geminate charge recombination within the solvent cage. Femtosecond transient absorption spectroscopy was performed using CH_3CN or CH_2Cl_2 and *N,N*-dimethylaniline (DMA) as the electron donor (**Figure 8**). In CH_2Cl_2 the LMCT excited state decayed concomitantly to the formation of charge separated species, confirming the electron-transfer nature of the excited-state quenching of $[Fe(phtmeimb)_2]^{+*}$ by the amine and yielding the corresponding electron transfer rate constant, k_{et} = 2.30 x10^{10} $M^{-1}s^{-1}$. The spectral signature of the charge separated state corresponded to those recorded by nanosecond transient absorption spectroscopy. In CH_3CN, the formation of such charge separated species was not observed. This was consistent with the low yield of charge separated products measured on the nanosecond time scale. The experiments indicate that the visible-light-mediated dehalogenation catalysis would be more efficient in dichloromethane compared to solvents of higher polarity and led to the optimization of the photoredox catalysis experimental conditions. Indeed, when the dehalogenation reaction was performed in CH_2Cl_2 in optimized catalytic conditions, 87% isolated yield was obtained for the photoredox catalytic process, whereas the yields decreased to 15%, 7%, 30% and 31% in acetone, BuCN, CH_3CN, and DMF respectively. The iron photosensitizer could be recycled with 88% yield after the photoreaction.

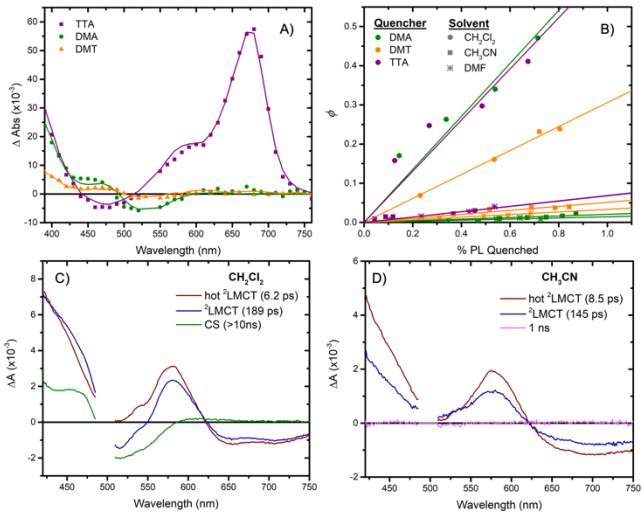

Figure 8. (a) Nanosecond transient changes recorded after pulsed 532 nm laser excitation in argon saturated CH_2Cl_2. Absorption changes were modelled (solid line) as a 1:1 sum of the reduced $[Fe(phtmeimb)_2]^+$ and oxidized quencher spectra obtained by spectroelectrochemistry. (b) Cage-escape yields for DMA (green), DMT (orange), and TTA (purple) in CH_2Cl_2 (circle), CH_3CN (square), and DMF (crossed square). (c,d) Femtosecond transient absorption changes recorded under argon after pulsed 500 nm laser excitation of $[Fe(phtmeimb)_2]^+$ in the presence of 0.35 M DMA in CH_2Cl_2 (c) and in CH_3CN (d). Reprinted with permission from reference[9b]. Copyright 2021 American Chemical Society.

Cage-escape yields were already studied in the literature,[9a-ai] but this report on the fact that cage-escape yields may impact reaction yields sparked a renewed interest in factors governing these cage-escape processes. Recently, we investigated the cage-escape yields of a series of inorganic photosensitizers with aryl-diazonium electron acceptors. We hypothesized that such compounds, which are known to irreversibly generate inert N_2 gas upon one electron reduction, would lead to increased ϕ_{CE} by hindering back electron transfer processes within solvent cage.[9c] This hypothesis turned out to be incorrect but allowed to estimate that the dissociation of the aryl-diazonium to release N_2 and the corresponding radical occurred on the short nanosecond timescale (less than 10 ns). The ϕ_{CE} were determined for $[Os(bpy)_3]^{2+}$, $[Ru(bpy)_3]^{2+}$, $[Ir((dFCF_3)ppy)_2(dtb)]^+$, $[Ir(ppy)_2(dtb)]^+$ and $[Ir(ppy)_3]$ with a series of aryl diazonium by using $[Ru(bpy)_3]^{2+}$ as actinometer. For $[Os(bpy)_3]^{2+}$ and $[Ru(bpy)_3]^{2+}$, the cage-escape yield increases from 18% to 98% along with the increasing driving force for electron transfer. For the iridium photosensitizers, ϕ_{CE} using 4-MeO-benzene diazonium were between 43% and 61% and reached value of 100% when the driving force was increased.

4. Time Resolved Infrared Spectroscopy

4.1. Technique overview

Time-resolved infrared (TRIR) spectroscopy is similar to transient absorption spectroscopy as changes in the IR region are monitored after UV-visible pulsed light excitation. This technique is particularly suited for the study of organic molecules bearing substituent that have clear IR signatures. In TRIR spectroscopy, the reaction is first optically triggered and then followed in time by sending in a broadband IR pulse and acquiring the corresponding IR spectra at different time delays to deduce the reaction dynamics. The intensity decay and rise of vibrational bands or the appearance of new IR bands gives information on the decay of reactants and formation of products. One of the main limitations of TRIR lies in the choice of solvent that also exhibit IR absorption features which can mask those of the substrate (for example, D_2O can be used as solvent instead of H_2O if it absorbs too strongly in the IR investigated region).[29] Other limitations, as will be presented herein, lie in the excited-state lifetime of the sensitizer and the cage-escape yields.

4.2. Selected examples from the literature

$[Fe(phtmeimb)_2]^+$ was investigated as PS in a benchmark dehalogenation reaction of 4-bromobenzyl-2-chloro-2-phenylacetate[9b] as reported by Stephenson et al. using $[Ru(bpy)_3]^{2+}$.[30] The step involving excited-state electron transfer from the quencher to the excited PS was previously described by nanosecond and femtosecond UV-Visible transient absorption spectroscopy. The reaction could be monitored by TRIR when dimethylaniline (DMA) was used as a quencher but not when triethylamine (TEA) was used. This is due to a combination of the short excited-state lifetime of $[Fe(phtmeimb)_2]^{+*}$ in combination to the moderate cage-escape yields obtained with TEA (0.21 ±0.05) compared to the one determined with DMA (0.60 ±0.09). When $[Ru(bpy)_3]^{2+}$ was used, the reaction with TEA could also be studied due to the longer excited-state lifetime, even with a low cage-escape yield. However, clear indications of ligand-loss chemistry were observed that is problematic for mechanistic investigations or for catalyst recyclability.

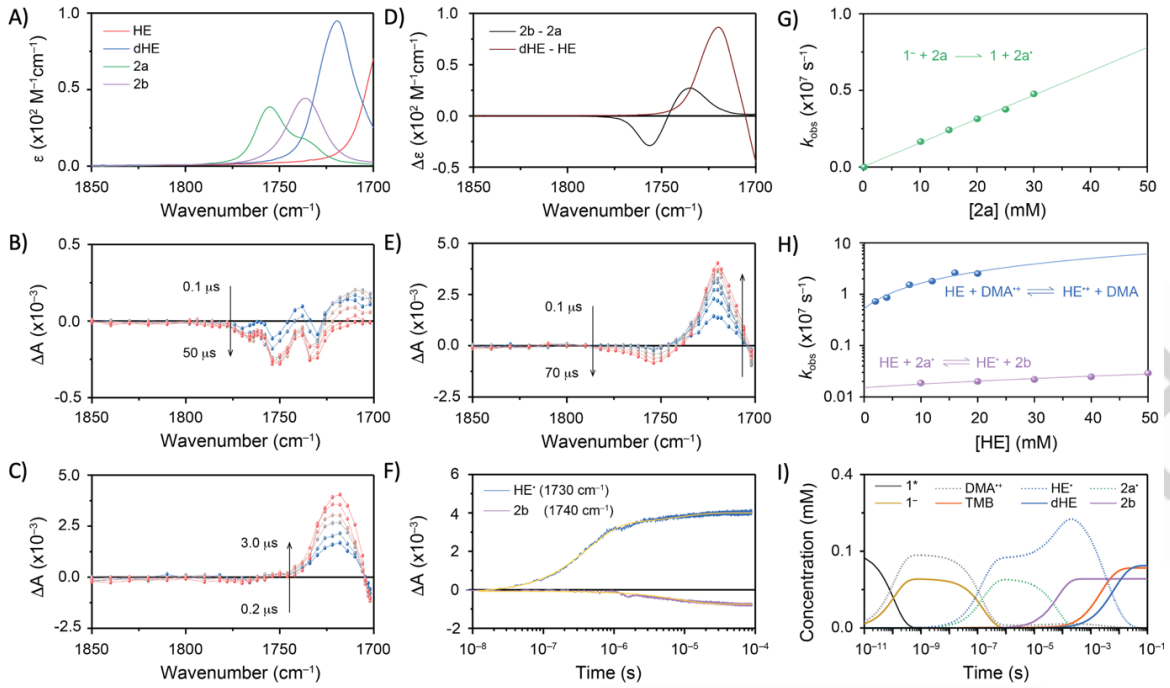

Figure 9. TRIR studies of the photo-initiated redox reactions. The following notation is used: 1 = $[Fe(phtmeimb)_2]^+$, HE = Hantzsch Ester, dHE = dehydrogenated HE, 2a = 4-bromobenzyl-2-chloro-2-phenylacetate, 2b = = 4-bromobenzyl-2-phenylacetate, DMA = N,N-dimethylaniline, TMB = N,N,N',N'-tetramethylbenzidine. (a) Fourier transform infrared (FTIR) spectra of the relevant substrates. TRIR absorption changes measured after a pulsed 500 nm laser excitation of solution mixtures containing (b) $[1^+]$ = 3 mM, [DMA] = 1 M, [2a] = 30 mM; and (c) $[1^+]$ = 3 mM, [DMA] = 1 M, [HE] = 30 mM. (d) Differential absorption changes expected for substrate transformations 2b → 2a and dHE → HE. (E) TRIR absorption changes measured after a pulsed 500 nm laser excitation of a solution mixture containing $[1^+]$ = 3 mM, [DMA] = 1 M, [HE] = 30 mM, [2a] = 30 mM. (f) Kinetic traces measured at the indicated wavenumbers that report on HE• and 2b formations. (g, h) Plots of the measured kinetic rate constants as a function of the indicated substrate concentrations. Overlaid to experimental data points are linear fits from which second-order rate constants were extracted. (i) Simulated time dependent concentrations of the indicated reaction components based on experimentally determined kinetic parameters. Reprinted with permission from reference[9b]. Copyright 2021 American Chemical Society.

As the first light-induced step was confirmed by transient absorption spectroscopy to occur via excited-state electron transfer, the subsequent electron transfer steps occurring from the mono-reduced photosensitizer could be investigated by TRIR. Electron transfer from the monoreduced PS to 4-bromobenzyl-2-chloro-2phenylacetate occurred with a rate constant of 1.6 x10^8 M^{-1} s^{-1}, which irreversibly induced heterolytic C–Cl bond breaking to yield the corresponding radical and (presumably) Cl^-. The dimerization of the sacrificial DMA electron donor was studied in details by Bard *et al*., and occurred with a rate constant of 2.5 x10^8 $M^{-1}s^{-1}$ in CH_3CN.[31] TRIR also provided evidence for a hydrogen atom transfer side reaction between Hantzsch ester and DMA•. This allowed to rationalize why slight excess of Hantzsch ester were needed for the reaction to go to completion.

TRIR experiments in conditions used for photoredox catalysis are shown in **Figures 9B-E**. The collective interpretation of the findings obtained from TRIR indicate that the overall photocatalytic process is dominated by two kinetically competing reaction equilibria (steps 3 and 4) that consume Hantzsch ester (**Figure 10**). Thankfully, the dimerization process of the DMA• to form TMB coupled to the conversion of HE• to dHE are two irreversible processes that drive the equilibria in the catalytic cycle towards the desired dehalogenated final product.

The reaction dynamics of the photoredox catalytic cycle shown in **Figure 9F-H** were simulated from numerical solutions of the coupled differential equations that describe the time dependent concentrations of all reaction components observed from the TRIR experiments. These simulations are shown in **Figure 9I** for the indicated reaction components. The biphasic formation of HE•, as described in steps 3 and 4 of the cycle in **Figure 10**, is readily observed. The bimolecular and concentration dependent kinetics for consumption of HE• and dimerization of $DMA^{\bullet+}$ largely control the final formation of dHE relative to phenylacetate product. In fact, the kinetic analysis in **Figure 9I** shows that dHE is formed in the presence of an excess of 1.3 times compared to dehalogenated product, a result that compares well with steady-state photoreaction experiments that required excess amounts of HE to ensure complete conversion of 4-bromobenzyl-2-chloro-2-phenylacetate.

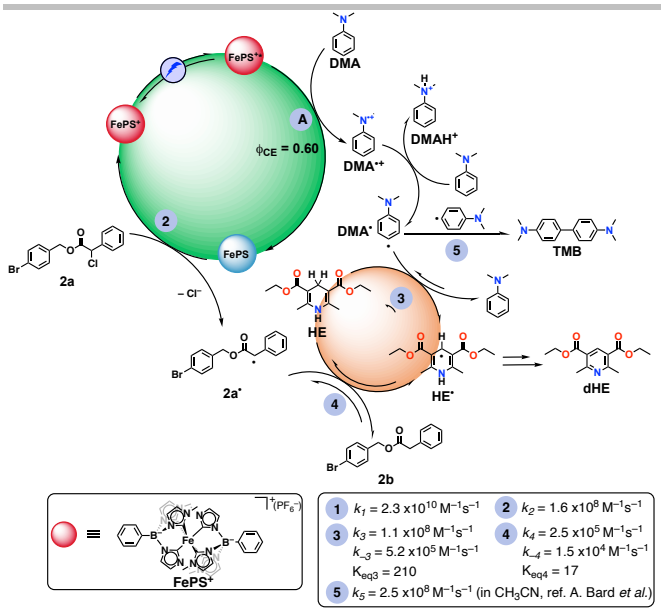

Figure 10. Proposed mechanism for the visible-light mediated dehalogenation of 2a to 2b in CH_2Cl_2 using $[Fe(phtmeimb)_2]^+$ as photosensitizer in the presence of DMA as a sacrificial electron donor and HE.[9b]

Another relevant example lies in the photosensitized dehalogenation/cyclization of dimethyl 2-bromo-2-(pent-4-en-1-yl)malonate (malonate-Br) using $[Ru(bpy)_3]^{2+}$ and $[Fe(phtmeimb)_2]^+$ as the photosensitizers.[9a] In experiments performed using conditions relevant to photoredox catalysis, pulsed light excitation of a solution containing $[Ru(bpy)_3]^{2+}$, TEA and malonate-Br resulted in absorption changes that were consistent with the consumption of malonate-Br, as evidenced by the bleach at 1744 cm^{-1}, and the formation of a cyclic product, as evidenced by a slower growth of a positive absorption change around 1728 cm^{-1} (**Figure 11**). The close resemblance of the IR spectra of both cyclic compounds precluded any critical differentiation of the formed products from TRIR experiments.

Overall, kinetic studies using $[Ru(bpy)_3]^{2+}$ were conducted in key spectral regions and analyzed under pseudo-first order conditions relative to the concentration of malonate-Br substrate, **Figure 11**. The kinetics measured were complex and globally treated with a tri-exponential model tentatively assigned to three sequential steps in the catalytic cycle: 1) electron transfer from PS^- to malonate-Br, 2) cyclization of linear-malonate• to form cyclic•, and 3) bromine atom transfer from malonate-Br to cyclic• to give the final product cyclic-Br.

These assignments were substantiated by the fact that rates measured in 1) and 3) were first-order in [malonate-Br] while the rate constants measured for 2) were concentration independent suggestive of an intramolecular chemical step. A second-order rate constant of 1.5 x10^8 $M^{-1}s^{-1}$ was obtained for electron transfer from the monoreduced $[Ru(bpy)_3]^+$ to malonate-Br, with the intramolecular cyclization step occurring with a rate constant of 1.5 x10^5 s^{-1}. The final step that produces cyclic-Br is slow with bromine atom transfer from malonate-Br to cyclic• occurring with a rate constant of 3.6 x10^6 $M^{-1}s^{-1}$. Kinetic analysis conducted with $[Fe(phtmeimb)_2]^+$ and DMA as the electron donor showed monophasic behavior that was first-order in [malonate-Br] with a second-order rate constant of 2.3 x10^8 $M^{-1}s^{-1}$ obtained for the electron transfer from monoreduced $[Fe(phtmeimb)_2]$ to malonate-Br.

Taken altogether, the data presented herein allowed to propose a plausible mechanism for the two photosensitizers (**Figure 12**). Light excitation of the PS yields an excited-state that is reductively quenched by triethylamine, $[PS^*,TEA] \rightarrow [PS^-,TEA^{+\bullet}]$. The reduced photosensitizer transferred an electron to malonate-Br, which induced heterolytic C–Br bond breaking to yield the linear-malonate• radical.

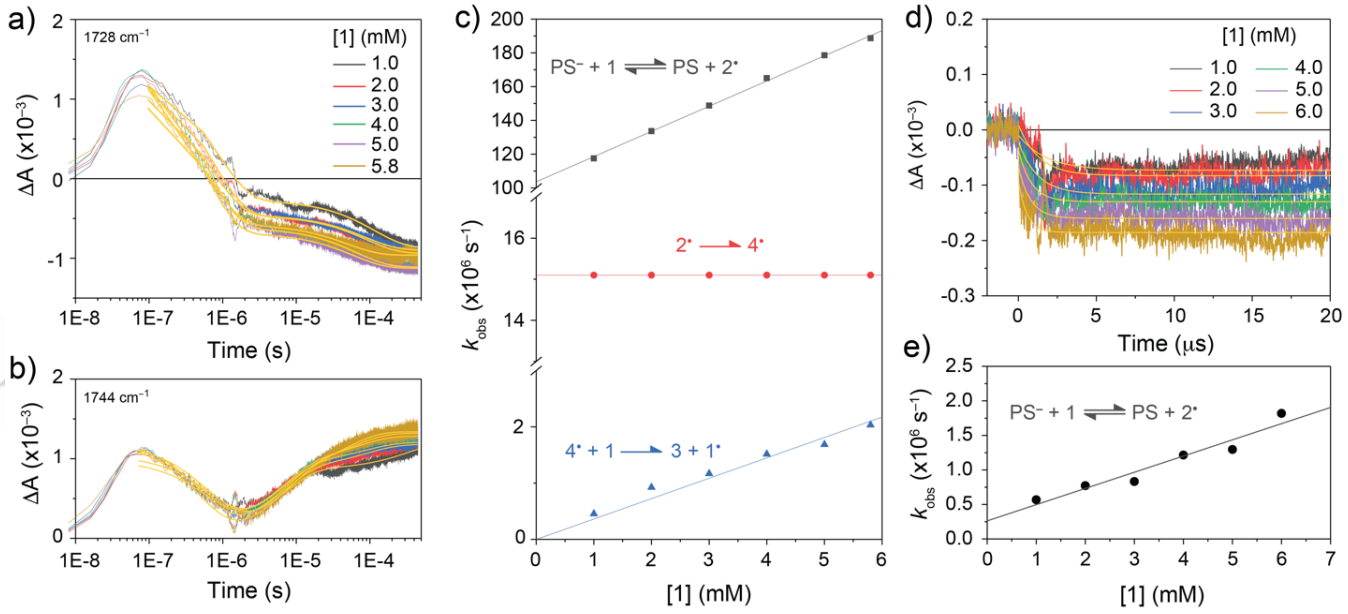

Figure 11. The following notation is used: PS = $Ru(bpy)_3]^{2+}$, 1 = dimethyl 2-bromo-2-(pent-4-en-1-yl)malonate, 2• = radical of dehalogenated 1, 3 = cyclic-Br product 4 = cyclic product (see **figure 11**). Absorption changes following pulsed 532 nm excitation of $[Ru(bpy)_3]^{2+}$ monitored at (a) 1728 cm^{-1} and (b) 1744 cm^{-1} with the indicated concentration of [malonate-Br] in CH_2Cl_2. (c) Pseudo first-order observed rate constants rates extracted from data in a) and (b) plotted against [malonate-Br]; the corresponding reaction chemistries are indicated for each dataset. (d) Absorption changes measured at 1728 cm^{-1} for $[Fe(phtmeimb)_2]^+$ following pulsed 532 nm laser excitation at the indicated concentration of 1. (e) Pseudo first-order observed rate constants rates extracted from data in d) plotted against the concentration of 1. Reproduced from reference [9a] with permission from the Royal Society of Chemistry.

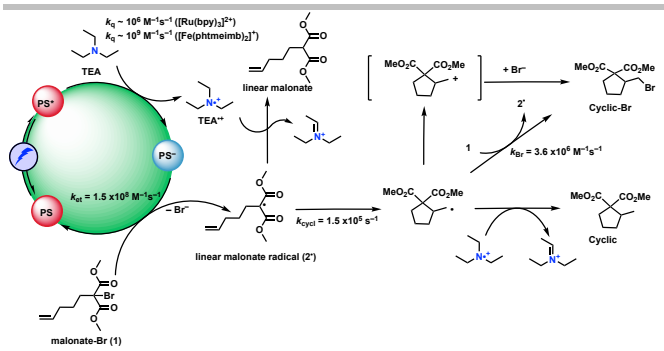

Figure 12. Proposed mechanism for the visible-light mediated dehalogenation of malonate-Br.[9a]

5. X-Ray Transient Absorption Spectroscopy

5.1. Technique overview

X-ray transient absorption spectroscopy (XTAS) follows the same pump-probe scheme than classical transient absorption spectroscopy, using a laser pulse to trigger the formation of a transient species and a time delayed X-ray pulse to probe the transient electronic and geometric structures around X-ray absorbing atoms. XTAS is based on the steady-state X-ray absorption spectroscopy (XAS), including X-ray absorption near edge structure (XANES) and extended X-ray absorption fine structure (EXAFS). The main difference between classical transient absorption spectroscopy and XTAS lies in the fact that the pump and the probe pulse induce two different absorption processes that are not coupled coherently due to their high photon energy difference (~2 eV for the laser pulse and ~7 keV for the X-ray probe).[32] The inner shell to valence orbital transitions induced by highly energetic X-ray photons provides a new sets of electronic transitions correlated with electronic configurations of X-ray absorbing atoms. During photoredox catalysis, transition metals centers undergo oxidation, spin state and chemical environment changes in which electronic configurations of frontier orbitals are altered. Such changes frequently lack distinct features in the visible light region or are masked by strong electronic transitions such as ligands centered π to π^* transition. Moreover, as the atomic ionization energy (energy required to remove an electron from an atom) depends on the atomic number, XTAS allows the specific analysis of an element, which renders XTAS a powerful method to identify electronic configurational changes at specific metal centers induced by visible-light excitation.[33] This powerful technique allowed to study the excited state structure of light-absorbing molecules[34] as well as to decipher the mechanisms and kinetics of photoinduced CO_2 reduction[35], water oxidation[36] and reduction[37] and organic synthetic[38] processes.

5.2. Selected examples from the literature

In their study of a light-induced hydrogen evolution reaction catalyzed by a tetradentate macrocyclic cobalt complex $[LCo^{III}Cl_2]^+$, photosensitized by $[Ru(bpy)_3]^{2+}$ in the presence of an equimolar mixture of sodium ascorbate/ascorbic acid in pure water, Southworth and co-workers used XTAS at the Co K-edge to follow the dynamic processes of the full catalytic cycle, using the element selectivity of XTAS to monitor changes related to the cobalt species without any contributions from $[Ru(bpy)_3]^{2+}$ or organic compounds.[39]

In this system, a spontaneous "dark" reduction from Co(III) to Co(II) is performed using sodium ascorbate.[40] This "dark" process was confirmed by XAS analysis of a mixture of $[LCo^{III}Cl_2]^+$ and $H_2Asc/NaHAsc$, showing the expected energy shift in the XANES region when compared to the Co(III) complex.

XTAS of the catalytic mixture in water showed the formation and decay of at least two different cobalt species in the nanosecond to microsecond time scale (**Figure 13A-B**). After visible light excitation, a reduced species is formed within a few nanoseconds with a peak at 7714 eV in the differential spectrum, pointing towards the formation of a Co(I) complex. This reduced species has a lifetime of 1.75 μs as determined from the kinetic trace obtained at different time delays (**Figure 13C**). In order to identify the structure of this reduced complex, XANES spectra of different Co(I) models were simulated and used to calculate the difference spectrum by subtraction with the Co(II) square pyramidal spectrum. Molecular orbital DFT calculations for a Co(I) square planar geometry reproduced well the pre-edge peak characteristic of the Co(I) at 7714 eV. As the simulated spectra finely matched the experimental one, it was concluded that the probable geometry for the reduced species formed after laser excitation was a Co(I) square planar complex.

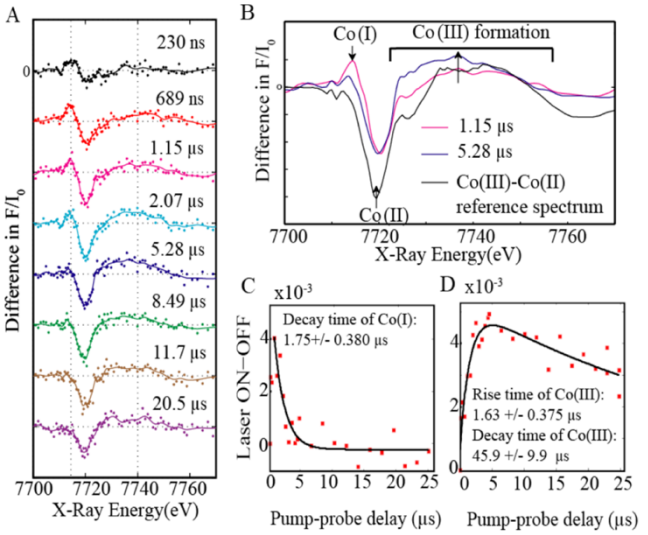

Figure 13. Co K-edge X-ray transient absorption spectra of an aqueous mixture containing $[LCo^{III}Cl_2]^+$ (6 mM), $[Ru(bpy)_3]^{2+}$ (30 mM) and $H_2Asc/NaHAsc$ (1:1, 214 mM). (a) Stacked spectra corresponding to a series of time delays between laser and X-ray pulses. These measurements were carried out for a range of averaged time delays from 0 to 25 μs. Each transient signal represents an average of a set of delays over 459 ns. (b) Selected transient spectra showing the Co(I) decay and Co(III) formation in the 1.15 μs (magenta) and 5.28 μs (blue) time delays. In black, the inverse of the transient spectrum obtained for binary mixtures $[LCo^{III}Cl_2]^+/[Ru(bpy)_3]^{2+}$ corresponding to the Co(III) to Co(II) transformation. (c) X-ray kinetics taken at 7713.9 eV of a ternary mixture $[LCo^{III}Cl_2]^+/[Ru(bpy)_3]^{2+}/Asc$, corresponding to the decay of the Co(I) photoinduced species (red dots) with the corresponding kinetics fitting (black solid line). (d) X-ray kinetics taken at 7732.9 eV of a ternary mixture $[LCo^{III}Cl_2]^+/[Ru(bpy)_3]^{2+}/Asc$, corresponding to the formation and decay of the Co(III) photoinduced species (red dots) with the corresponding kinetics fitting (black solid line). The decay of the Co(I) species has been fitted using an exponential function. The rise and decay of the Co(III) species have been fitted by using a system of ordinary differential equations with three parameters: the rise rate, the decay rate, and the population of the excited transient Co(I) species. Reprinted with permission from reference [39]. Copyright 2016 American Chemical Society.

While the Co(I) intermediate decays in the measured transient spectra, a second oxidized species is formed, as showed by a broad band appearing in the energy range of 7720-7750 eV (**Figure 13A**). The formation of this intermediate has a rise time of 1.63 μs that correlates with the observed Co(I) lifetime of 1.75 μs, indicating that both processes are linked to the same reaction step. Several mechanisms were considered. The first one involved the protonation of Co(I) to the corresponding Co(III) hydride that can yield hydrogen by reacting with a proton. Alternatively, the Co(III) hydride can produce hydrogen via a homolytic pathway through a reaction with a second equivalent of Co(III) hydride.[41] Another mechanism would involve the reduction of Co(III) hydride to the corresponding Co(II) hydride that can react according to the two above-mentioned mechanisms. Simulation of XANES spectra of the possible Co(II) and Co(III) hydride species was performed. A comparison with experimental spectra indicated that the best agreement was found for the Co(III) octahedral geometry with two aqua axial ligand $[LCo^{III}(OH_2)_2]^{3+}$ formed at longer experimental times, pointing toward a mechanism for hydrogen production involving a Co(III) hydride species. It was proposed that the formation of the hydride intermediate was the rate determining step and that this species could then rapidly react with a proton to form H_2 and regenerate the starting $[LCo^{III}(OH_2)_2]^{3+}$ within a timescale of <2 μs.

6. Laser Pulse Radiolysis

6.1. Technique overview

Laser pulse radiolysis (PR) utilizes short and intense pulses of ionizing radiation (photolysis) or of MeV electron pulses (radiolysis) that induce solvent ionization. The ionized solvent is then able to perform electron or hole transfer to the solutes of interest. This is coupled to time resolved absorption spectroscopy of the generated oxidized or reduced transient species. The technique thus combines the precision of ultrafast laser technology with the insights of radiolysis to investigate the dynamics of radiation-induced chemical processes. This approach allows to probe the intricate details of chemical reactions occurring on ultrafast timescales and was involved in various fields such as photoredox chemistry and molecular biology.[42]

A typical PR setup (**Figure 14**) consists of three main components: a radiation source, a laser system, and a detection system. The radiation source, often a pulsed electron beam or a gamma-ray source, generates a burst of ionizing radiation. The laser system produces a train of micro- or nanosecond laser pulses, which can be tuned to match the temporal profile of the radiation burst. The detection system, typically a time-resolved spectroscopic setup, captures the changes in the chemical system induced by the radiation and laser pulses.[42a] In chemistry, it has been used to study the dynamics of short radical reactions, electron transfer processes, and chemical kinetics.[43] Notably, the technique allowed the first observation of femtosecond solvation dynamics of hydrated electrons in water, which was achieved in 1987 by Migus *et al.*.[44] The technique has also been employed to investigate the behavior of biological molecules, such as DNA, proteins, and antioxidants, under radiation-induced conditions.[45] The main advantage of femtosecond PR lies in its ability to capture even ultrafast chemical events with high temporal resolution (pico- to femtosecond timescale can be reached), enabling the observation of short-lived intermediates and transient species. Additionally, the technique offers a non-invasive and controlled approach to study radiation-induced chemical processes. However, challenges remain in terms of data analysis, signal-to-noise ratio, and the need for sophisticated experimental setups. A limitation lies in the choice of solvent that might undergo photochemical or radiolytic decomposition upon exposure to the intense laser radiation, producing additional reactive species that can interfere with the desired reactions. Most of the studies are performed in water, dimethylsulfoxide or acetonitrile. [42a]

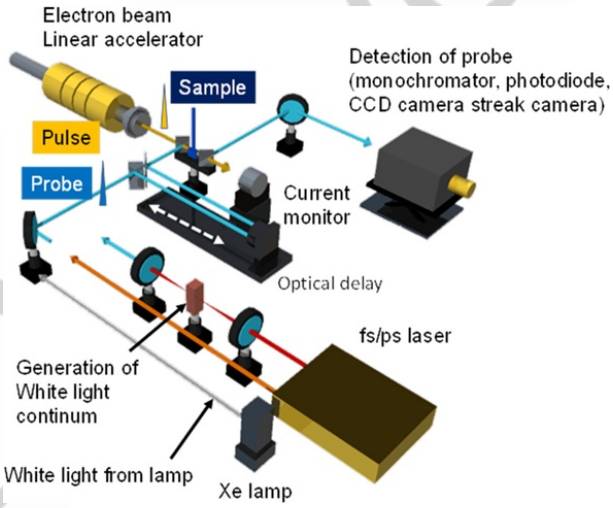

Figure 14. Laser pulse radiolysis setup. Reprinted with permission from reference [45b]. Copyright 2019 American Chemical Society.

6.2. Selected examples from the literature

In a recent study reported by Bird, MacMillan and co-workers, PR was used in combination with spectroelectrochemistry to generate and identify low-valent nickel intermediates relevant to dual Ir/Ni-photocatalyzed cross-coupling reactions.[46] Indeed, the initial step in most of these reactions involves an electron transfer from the Ir(III)* photocatalyst to the Ni(II) precatalyst (for example, ((dtbbpy)$NiBr_2$). Nevertheless, uncertainty persisted regarding the specific Ni species participating in the catalytic cycle. Examining the electrochemical reduction of (dtbbpy)$NiBr_2$ led to an irreversible process and subsequent chemistry due to a two-electron reduction. As a result, an alternative method was required.[47] The use of PR appeared to be relevant to generate and spectroscopically investigate Ni(I) intermediates. The recorded absorption spectra using a 9 MeV Laser Electron Accelerator Facility (the LEAF)[48] were very close to those obtained under electrolytic and synthetic condition (**Figure 15C**). The technique then allowed the observation of a rapid comproportionation process between Ni(0) and Ni(II) under synthetically relevant electrolysis conditions to generate bipyridine-ligated Ni(I).

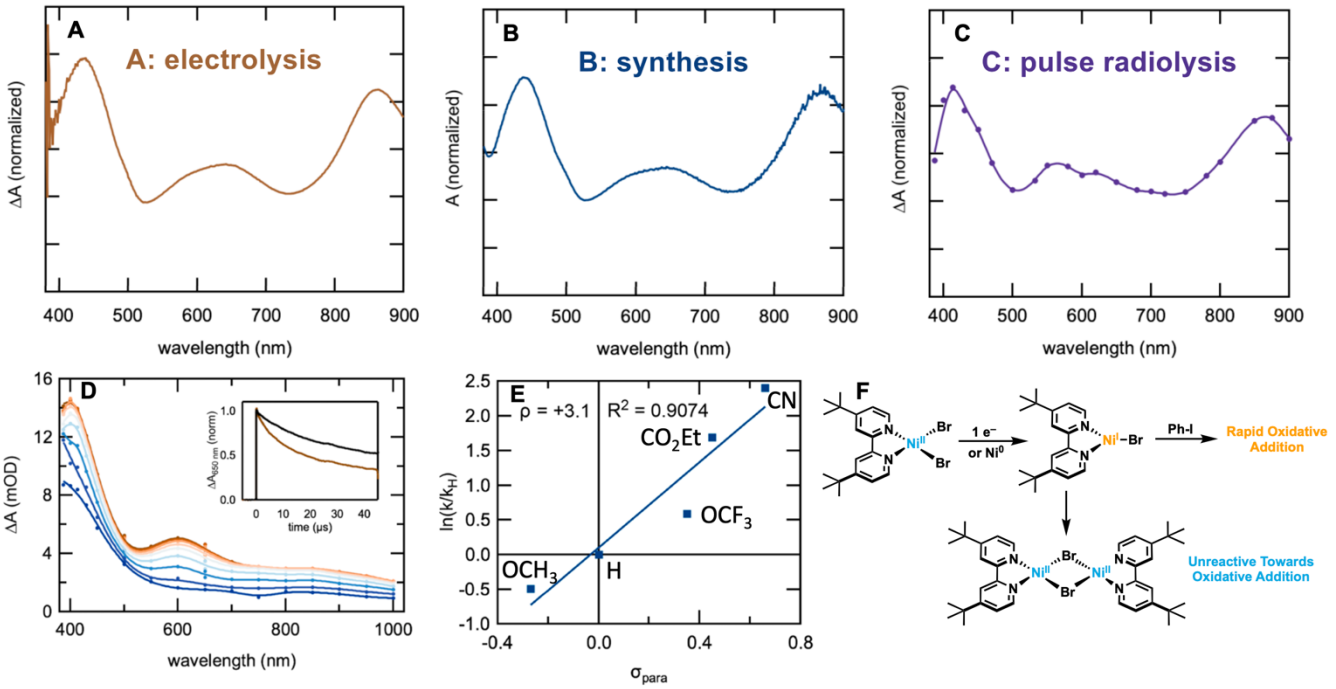

Figure 15. Normalized ΔA/A data for [(tpy)NiBe] generated by electrolysis (E_{app} = –750 mV vs SCE) (A), Stoichiometric synthesis (B) and pulse radiolysis (t = 100 ns) (C). Spectral evolution for Ni(I) signal in the presence of ethyl 4-iodobenzoate (500 mM) (D) and Hammett correlation demonstrating oxidative addition rate sensitivity to aryl iodide electronics (E). Adapted with permission from reference [46]. Copyright 2021 American Chemical Society.

Essentially, PR allowed for the direct observation and characterization of the Ni(I) species, providing valuable insights into their structure, reactivity, and electron transfer processes. The study therefore provided direct measurements of Ni(I) oxidative addition rates with electronically differentiated aryl iodide electrophiles, highlighting the significance of this organometallic step in nickel-catalyzed cross-coupling reactions. Various electronically differentiated 4-substituted aryl iodide derivatives were examined by pulse radiolysis which allowed to monitor the spectral changes associated with the decay of the Ni(I) species. **Figure 15D** displays the quenching of the Ni(I) signal when reacting with 4-iodobenzoate, one of the most reactive species of the series. A Hammett (*σp*) correlation clearly revealed the sensitivity of the oxidative addition rate to aryl iodide electronics. Indeed, plotting the $\ln(k_{OA}/k_{OA(H)})$ *vs* *σp* for the different 4-substituted iodoarenes showed an 18-fold increase in rate over the studied range (σ=−0.27 to +0.66) of the oxidative addition rate (**Figure 15E**).

The study also allowed to shine light on the factors influencing catalytic efficiency and selectivity by characterizing the short-lived Ni(I) species lifetimes, reaction kinetics, and stability, which are critical for understanding the underlying mechanisms of cross-coupling reactions. Indeed, as presented in **Figure 15F**, the transiently generated [(dtbbpy)NiBr] complex reacts quickly with iodobenzene, while the dimeric form, $[(dtbbpy)NiBr]_2$ appeared to be virtually unreactive. This was shown by monitoring the reaction between synthesized dimer and iodobenzene through ^{1}H-NMR analysis. No conversion of iodobenzene was noticed which contrasts with the high reaction rate for the monomeric complex measured through pulse radiolysis (k_{OA}= 2.2 (±0.3)×10^{4}M^{-1}s^{-1}). This may explain why high concentrations of low-valent Ni are thought to be deleterious for the reaction rate, given the kinetic favorability of dimer formation under such conditions.

The ultrafast time resolution and high sensitivity of PR enabled the detection and analysis of transient species, offering a unique opportunity to study Ni(I) intermediates. Initiating the radiolysis process with precise timing allowed to explore the reaction kinetics for the determination of rate constants associated with various steps of the catalytic cycle, including ligand exchange, oxidative addition, and reductive elimination. This kinetic data aids in understanding the factors affecting reaction rates and designing more efficient catalytic systems. This provided mechanistic insights into the pathways and steps leading to the formation of desired coupling products.

As presented in this example, PR holds a significant place in the field of radiation chemistry by providing a unique tool to investigate the dynamics of chemical reactions on ultrafast timescales. Its ability to capture transient species and elucidate reaction mechanisms has opened new avenues for understanding the fundamental processes induced by ionizing radiation. With continued advancements in ultrafast laser technology and data analysis techniques, PR holds great promise for future discoveries and applications in various scientific disciplines.

7. Photo-CIDNP Spectroscopy

7.1. Technique overview

CIDNP, or Chemically Induced Dynamic Nuclear Polarization, is a phenomenon in which non-Boltzmann nuclear spin states are produced in thermal or photochemical reactions through

colligation, diffusion, or disproportionation of radical pairs. This effect was first observed independently in the late 1960s by Bargon, Fischer, Johnsen, Ward, and Lawler. Initially, the dynamic nuclear polarization aspect was explained by electron-nuclear Overhauser effects, but later, Closs, Kaptein, and Oosterhoff proposed a radical pair mechanism that relied on electron-nuclear spin interactions to alter the recombination probability of radical pairs.[49] The reader is referred to literature for general and more comprehensive descriptions of the technique.[49-50]

The basic processes involved in the production of photo-CIDNP are summarized in **Figure 16** for a reductive quenching process. The photosensitizer (PS) is promoted to a singlet excited state (^{1}PS*) by light absorption and reaches a triplet excited state (^{3}PS*) *via* intersystem crossing. For Ru(II) polypyridine complexes, the quantum yield of intersystem crossing between the ^{1}MLCT and ^{3}MLCT excited states is 100 %. Reductive quenching of this triplet excited state yields a triplet radical pair, referred to as $^3\{P^{\bullet-}Q^{\bullet+}\}$, which separates into free radicals (escape radicals) unless a competing event occurs during its lifetime. In cyclic photoreactions, this event consists of triplet to singlet conversion followed by back electron transfer, yielding the so-called geminate recombination products, i.e. the diamagnetic parent compounds. The spin-orbit coupling is the primary cause of intersystem crossing, but this does not yield CIDNP. Hyperfine couplings may also induce triplet to singlet interconversion and this mechanism is responsible for nuclear spin-state sorting (also simply referred to as spin sorting). Accordingly, a fraction of the geminate recombination products and the corresponding amount of free radicals (escape radicals) are generated with equal but opposite nuclear polarizations, which are simply referred to as escape and geminate polarizations. Escape polarizations are carried out by paramagnetic species and are therefore rather short-lived. They are strongly reduced by nuclear relaxation before the diamagnetic parent compounds are finally recovered by random recombination.

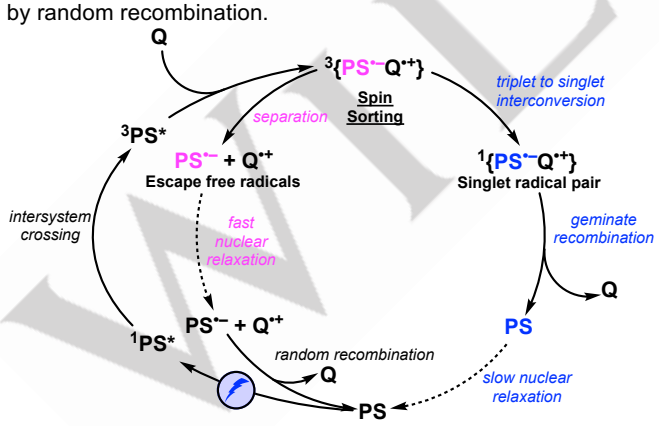

Figure 16. Basic processes involved in CIDNP production for a cyclic photoreaction for a reductive quenching process. PS stands for the photosensitizer and Q for the quencher. Proton transfer and self-exchange processes are not represented. Species generated with a non-Boltzmann nuclear spin state distribution are colored in magenta (escape polarization) or blue (geminate polarization). The spin sorting process is illustrated with nuclear polarization on PS. Besides, it is considered that fast paramagnetic nuclear relaxation annihilates the escape polarization before random recombination and, consequently, that no cancellation of the geminate polarization occurs. Polarization arising from so-called F-pairs, i.e., radical pairs formed by random reencounter of free radicals, is also ignored.[51]

In contrast, geminate polarizations are carried out by diamagnetic species, which are characterized by much longer ^{1}H longitudinal relaxation times. Hence, geminate polarizations that are produced on the 10^{-9}-10^{-10} s timescale can be detected much later by NMR. As Boltzmann equilibrium at room temperature corresponds to almost equipopulated nuclear spin states, significant signal enhancements can be detected even though the spin sorting process is not very efficient. Photo-CIDNP enhancements can be positive or negative, depending on the sign of the hyperfine coupling constant notably, and can be observed for both the photosensitizer and the quencher.

Geminate polarizations exhibit long relaxation times and can be easily detected using NMR, while escape polarizations are short-lived and rapidly produce the parent compound by random recombination. The probability of a given radical pair to yield geminate or escape products depends on their nuclear spin state, which is influenced by the hyperfine coupling. The hyperfine coupling intersystem crossing (HF-ISC) favors the geminate pathway for one population of nuclear spin, the α state. The sign of observable photo-CIDNP enhancements is influenced by the hyperfine coupling constant, and these enhancements can be observed on either the photosensitizer or the quencher. A steady-state photo-CIDNP setup is shown in **Figure 17**. It consists in performing classical NMR measurements using an optical fiber insert and a coaxial insert which allows the continuous irradiation of the sample during the acquisition of the NMR spectrum.

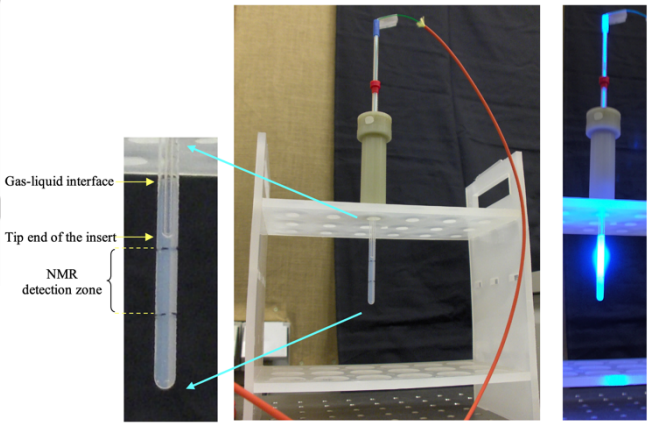

Figure 17. Steady-state photo-CIDNP setup involving optical fiber insert. Reprinted with permission from reference [51b]. Copyright 2017 American Chemical Society.

Most studies reported to date make use of photo-CIDNP as a tool to investigate the surface structure of proteins, protein folding as well as recognition processes and organic reaction mechanisms.[50a, 52] Of particular interest for this concept article is the use of photo-CIDNP to investigate electron transfer with transition metal complexes. There have only been a few reports of the use of this technique with reactions involving ruthenium(II) polypyridyl complexes, yet the atomic resolution provided by NMR spectroscopy makes it a very valuable and promising tool. [51a, b, 53]

7.2. Selected examples from the literature

In a recent study, ruthenium(II) photosensitizers such as $[Ru(TAP)_2(phen)]^{2+}$, $[Ru(TAP)_3]^{2+}$ or $[Ru(TAP)_2(HAT)]^{2+}$, (where

phen is 1,10-phenanthroline, TAP is 1,4,5,8-tetraazaphenanthrene and HAT is 1,4,5,8,9,12-hexaazatriphenylene) were investigated for their visible light induced reactivity at various pHs with quenchers that include hydroquinone (H_2Q), N-acetyl-tyrosine (N-Ac-Tyr) and guanosine 5'-monophosphate (GMP). For $[Ru(TAP)_3]^{2+}$, it was shown that a photo-induced electron transfer was possible. At pH values greater than 5, excited-state electron transfer occurred primarily with the non-protonated form of the excited photosensitizer. For pH values > 7, photo-CIDNP effects were observed for the different quenchers, but not for the photosensitizer due to electron self-exchange that led to strong longitudinal relaxation enhancement which prevented the buildup of non-equilibrium magnetizations. Indeed, the absence of CIDNP enhancements does not always imply the absence of the generation of radicals as other factors can influence these enhancements.

At acidic pH, GMP was protonated and became an inefficient quencher, which led to the disappearance of photo-CIDNP enhancements. Interestingly, the excited-state electron transfer still occurred at pH < 1 with H_2Q or N-Ac-Tyr. This was very surprising as protonation of the excited-state would be expected at this pH, leading to a very short excited-state lifetime that would not compete with diffusional electron transfer. Clear difference in behavior could be observed for H_2Q and N-Ac-Tyr at low pH. Indeed, for hydroquinone, the photo-CIDNP enhancements reached a maximum around pH 5 and then decrease to enhancements around 80% at pH <1. For N-Ac-Tyr, the photo-CIDNP enhancements seemed quite constant for all values of pH < 5. For hydroquinone, experimental data confirmed that the excited-state electron transfer process was diffusion limited at pH ~5. The decrease observed at lower pH values mostly stemmed from a decrease in overall photo-induced electron transfer quantum yield because of the shorter excited-state lifetime. For N-Ac-Tyr, two antagonistic effects were proposed. The decreased excited-state lifetime induced by protonation, which decreases the quenching efficiency, and the increased driving force, also induced by protonation, which enhances the quenching rate constant toward the diffusion limit.

Most of the photo-CIDNP enhancements on $[Ru(TAP)_3]^{2+}$ were observed on the H-2,7 positions, independently on protonation. These positions were also identified by DFT calculations as those exhibiting the largest electron-spin density. However, protonation became a very important aspect when considering the excited-state reactivity of $[Ru(TAP)_2(HAT)]^{2+}$, with hydroquinone, N-Ac-Tyr and GMP. This photosensitizer contains non-equivalent protonation sites. At pH ~5, photo-CIDNP enhancements are primarily observed on the HAT H-2,7 position and, to a lesser extent, on the TAP H-2, 7 positions as displayed in **Figure 18**.

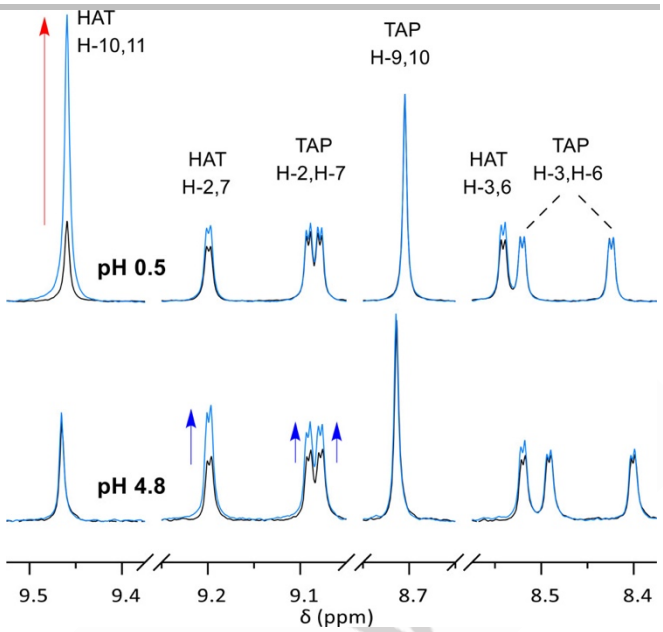

Figure 18. Regions of ^{1}H NMR spectra showing the signals of $[Ru(TAP)_2(HAT)]^{2+}$ for samples containing 2 mM H_2Q at pH 4.8 and 0.5. Equilibrium spectra are in black, and the spectra recorded with sample illumination are superimposed in blue. Reprinted with permission from reference [51b]. Copyright 2017 American Chemical Society.

Surprisingly, when the pH was decreased to values <1, drastic photo-CIDNP enhancements were observed on the HAT H-10,11 positions. Hence, it was proposed that two distinguishable photoinduced electron-/proton-transfer processes could be observed as a function of pH. For pH values greater than 1, excited-state electron transfer occurred between the quencher and the unprotonated excited photosensitizer. This electron transfer is followed by a proton transfer step within the geminate radical, preferentially on the HAT N-1,8-positions. At pH values under 1, excited-state electron transfer occurs from the quencher to the protonated excited photosensitizer. It is proposed that excited-state protonation occurred on the HAT N-9,12 positions. These observations were in line with electron-spin densities calculated by DFT (**Figure 19**).

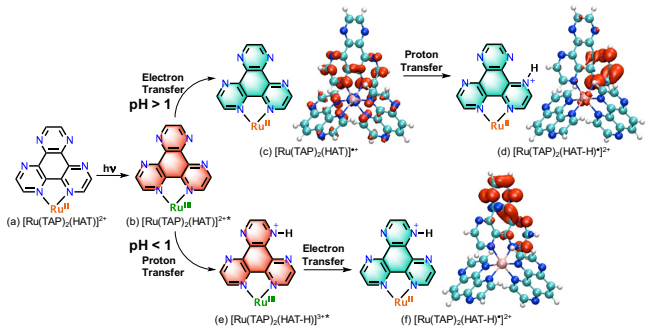

Figure 19. Photo-induced electron/proton transfer processes with the protonatable Ru(II) polyazaaromatic complex $[Ru(TAP)_2(HAT)]^{2+}$. For clarity reasons, the TAP ligands are only indicated for the figures showing the electron-spin density calculated by DFT. (a) ground state complex, (b) unprotonated ^{3}MLCT excited-state complex, (c) unprotonated monoreduced complex, (d) monoreduced complex protonated on a proximal nitrogen atom (N-1 or N8) of the HAT ligand, (e) excited-state complex protonated on a remote nitrogen atom (N-9 or N-12) of the HAT ligand and (f) corresponding monoreduced protonated complex. Reprinted with permission from reference [51b]. Copyright 2017 American Chemical Society.

8. Time-Resolved Electron Paramagnetic Resonance

8.1. Technique overview

The fundamental principle of Electron Paramagnetic Resonance (EPR) is akin to NMR spectroscopy. The main difference lies in the relaxation rates which are orders of magnitudes higher for electrons than for nuclei. EPR involves the application of an external magnetic field and microwave radiation to paramagnetic samples, inducing transitions between electron spin energy levels.[54] While traditional EPR focuses on obtaining a static EPR spectrum to reveal information about the sample's electronic structure, time-resolved Electron Paramagnetic Resonance (TR-EPR) allows to investigate how these electron spin levels change over time in response to various stimuli or conditions on timescales ranging from nanoseconds to milliseconds. TR-EPR therefore provides insights into the dynamic behavior of paramagnetic species in various environments. This technique has already been implemented for a broad range of applications across different scientific disciplines.[55] In biology, TR-EPR is employed to study biomolecules like proteins and enzymes, offering insights into their structural changes and electron transfer events with pulse-dipolar EPR expected to become a widely used technique.[56] Furthermore, TR-EPR has been applied to materials science to explore the properties of paramagnetic materials and nanoparticles, helping to design novel materials with specific magnetic properties.[57] TR-EPR also allows to investigate how the electron spin populations change during chemical reactions, shedding light on reaction kinetics and mechanisms, especially those involving radical intermediates, and electron transfer processes.[58] The TR-EPR setup includes several key components, such as a pulsed electron spin resonance spectrometer, a microwave source, a variable magnetic field, and a time-resolved detection system. The sample of interest is exposed to short and intense microwave pulses, which excite the electron spins, causing them to transition between energy levels.[55] By varying the time delay between the microwave pulse and the detection window, researchers can capture the transient changes in the EPR signal over time. The most utilized instruments employ continuous wave (CW) microwave irradiation at a frequency of 9 GHz. In recent years, various TR-EPR methods such as ESEEM, HYSCORE, and PELDOR have expanded the standard range of EPR techniques. Today, these hyperfine and dipolar methods can be applied to characterize not only the paramagnetic center itself but also its ligand environment and interactions with other EPR-active centers located up to 8 nm away.[56a]

The primary advantage of TR-EPR is its ability to provide detailed information about the dynamics of paramagnetic species. Capturing transient changes in the EPR signal allows to gain a deeper understanding on how electron spins interact with their environment. However, TR-EPR also presents challenges. The experimental setup can be complex and requires precise synchronization of microwave pulses, magnetic fields, and time-resolved detection systems. Noise and signal-to-noise ratio issues can affect the quality of the data, requiring sophisticated data processing techniques. Additionally, TR-EPR is limited to paramagnetic species. [55]

8.2. Selected examples from the literature

Ji and coworkers recently reported the use of TR-EPR spectroscopy to study C(sp^3)–H activation reaction.[59] Indane was selected as a model substrate that was reacted in continuous flow with a photo-enhanced phthalimide-N-oxyl (PINO) derivative that acted as hydrogen atom-transfer (HAT) mediator (**Figure 20D**). Indane reacted with O_2 in the presence of the $[Ir(dF(CF_3)ppy)_2(4,4'\text{-}CF_3bpy)]PF_6$ photosensitizer and $CuCl_2$ in CH_3CN under irradiation, yielding the desired oxidation product 1-indanone in 88% yield at 50°C. TR-EPR spectroscopy in combination to HRMS analysis allowed the observation of various intermediate species and the determination of the reaction kinetics. *Operando* EPR first highlighted that long-lived PINO radicals can be efficiently produced thanks to the Ir–Cu system. The EPR signal provided by the capture of the superoxide anion by DMPO (**Figure 20A**) allowed to investigate the activation of C(sp^3)–H by PINO radicals which was found to proceed with a rate constant of approximately 2.5 x 10^6 s^{-1}. The use of HRMS analysis also allowed to confirm the capture of indane's carbon-radical by DMPO as depicted in **Figure 20B**. EPR was also implemented to follow the rapid decline of the PINO radical which was correlated to the generation of indane's carbon radical as shown in **Figure 20C**. This suggested that the quenching of the PINO radical by indane led to the production of carbon-radicals.

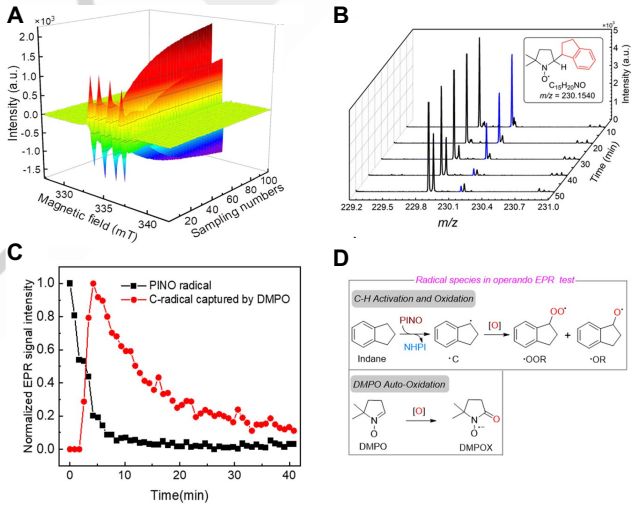

Figure 20. TR-EPR and HRMS findings from free radical trapping experiments. *In situ* EPR Visualization in 3D. (A) For the TR-EPR experiments conducted under operando irradiation, the reaction solution was mixed with DMPO and introduced into a flat cell. (B) The time-resolved HRMS results exhibit the capture of C-radicals by DMPO, as indicated by the blue line. (C) The evolution of normalized EPR intensity for both the PINO radical and DMPO-captured C-radical over time. (D) Radical species involved in the operando EPR tests are explored, including C–H activation, oxidation processes, and DMPO auto-oxidation. Reproduced from ref [59] with permission from the Royal Society of Chemistry.

The lifetime of the reaction intermediates was also investigated by TR-EPR. For instance, the PINO radical exhibited a characteristic lifetime of about 12 ns under the reaction conditions. The study highlighted the impact of light on the C(sp^3)–H activation. In particular, the photo-induced radical generation process resulted in a 3-fold enhancement in the reaction rate compared to the dark reaction. Finally, the quantum yield of the C(sp^3)–H activation process, determined using TR EPR, was found to be 0.35, indicating the efficiency of the reaction under the given conditions. In conclusion, the application of TR-EPR

spectroscopy has not only enabled a comprehensive understanding of C(sp^3)–H activation but has also provided precise quantitative data that elucidates reaction kinetics, intermediate lifetimes, radical concentrations, and the influence of light. The use of TR-EPR may therefore allow to advance the field of photoredox catalysis by providing mechanistic insight into these light-induced transformations. TR-EPR also comes with some challenges that are mostly related to the complex instrumentation, sample compatibility and the data analysis complexity.

9. Photoacoustic Spectroscopy

9.1. Technique overview

Modern photoacoustic (PA) spectroscopy combines the principles of laser pulse technology and of highly sensitive microvibrations detection to analyze the characteristics of materials. It utilizes laser pulses to induce a PA effect in a sample, which results in the generation of acoustic waves allowing the detection of low concentrations of analytes and the fine differentiation between different substances based on their absorption spectra. This technique has gained significant attention recently in various fields, such as environmental monitoring, biomedical imaging, and gas sensing.[60]

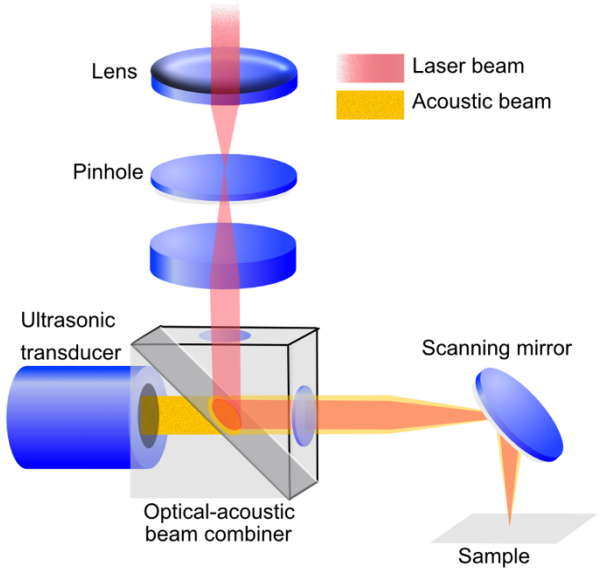

Figure 21. Scheme of a reflection-mode optical resolution (OR)-PAM system, featuring an optical-acoustic beam combiner that reflects light but transmits sound.

PA spectroscopy thus operates based on the principle of the PA effect discovered by Alexander Graham Bell.[61] When a sample absorbs laser pulses, it undergoes rapid thermal expansion, leading to the creation of pressure waves in the surrounding medium. These pressure waves can be detected using a highly sensitive microphone or other acoustic detection methods. By analyzing the amplitude and frequency of the detected acoustic waves, valuable information about the sample's optical absorption properties can be obtained. A typical PA spectroscopy setup consists of several key components. First, a pulsed laser source is used to generate short and intense laser pulses of a specific wavelength. This laser light is directed onto the sample of interest, which can be a solid, liquid, or gas. As the sample absorbs the laser pulses, the resulting pressure waves are detected by a sensitive acoustic detector, such as a microphone or an optical interferometer. **Figure 21** illustrates the schematic of a more sophisticated system used in PA imaging for high optical resolution featuring an optical-acoustic beam combiner that reflects light but transmits sound. The detected acoustic signals are then processed and analyzed to determine the sample's absorption spectrum.[62] PA is thus an indirect technique as an effect of absorption is measured rather than the absorption itself.[63]

PA spectroscopy has a wide range of applications across different scientific and technological fields. In environmental monitoring, it is used to detect and quantify pollutants in air and water samples, providing valuable information for pollution control and assessment (e.g. water contamination by chemical contaminants, suspended microplastics, and green algae colonies or CO, NH_3, NO, and CH_4 air pollutants in automotive industry).[64] In biomedical imaging, PA spectroscopy enables non-invasive imaging of tissues and organs, offering potential applications in cancer diagnosis and monitoring.[60a, c] Additionally, this technique has been implemented in gas sensing applications for the detection of trace gases in various industrial and environmental settings.[60b, 65]

One of the significant advantages of PA spectroscopy is its ability to provide sensitive and selective measurements of the absorption properties of samples. It allows for the detection of low analyte concentrations and can differentiate between different substances based on their typical absorption spectra. Furthermore, PA spectroscopy can be applied to a wide range of sample types, including solids, liquids, and gases.

However, there are certain challenges associated with PA spectroscopy. One challenge is the need for careful calibration and accurate determination of the signal-to-noise ratio to ensure reliable measurements. The sensitivity of the technique can be affected by various factors such as background noise, laser fluctuations, and acoustic interferences. Additionally, the interpretation of the acquired data requires sophisticated mathematical modeling and analysis techniques to extract meaningful information about the sample's composition and properties.

9.2. Selected examples from the literature

As mentioned above, PA spectroscopy revealed to be particularly interesting for high resolution imaging of tissues and organs and is reported as an emerging tool in clinical oncology.[62] A recent work of Lin and co-workers focused on application of Photoacoustic Computed Tomography (PACT) as a non-invasive imaging technique for monitoring breast cancer response to neoadjuvant chemotherapy. The study aimed to assess the effectiveness of PACT in capturing tumor changes during treatment and to highlight its potential advantages over conventional imaging techniques. The research employed a robust methodology, including patient cohorts, PACT image acquisition, and comprehensive data analysis.

Neoadjuvant chemotherapy is an important treatment approach for breast cancer, but accurately monitoring tumor response can be challenging. Traditional imaging techniques, such as mammography and ultrasound, have limitations in accurately characterizing tumor changes. PACT offers a promising alternative, combining the advantages of high-resolution imaging and functional information. The study enrolled a cohort of breast cancer patients undergoing neoadjuvant chemotherapy. PACT imaging was performed at multiple time points: before treatment initiation, mid-treatment, and after treatment completion. The obtained PACT images were analyzed to evaluate tumor volume, vascularization, and oxygenation levels. The results of this study demonstrated the potential of PACT in monitoring tumor response to neoadjuvant chemotherapy. PACT provided detailed information about tumor characteristics, including its size, vascularity, and even oxygenation levels. In **Figure 22**, the overall changes in tumor volume, vascularization, and oxygenation levels are visually presented. These changes highlight the dynamic nature of tumor response to neoadjuvant chemotherapy. PACT demonstrated its capability in capturing these changes, allowing clinicians to track treatment progress and make informed decisions.[66]

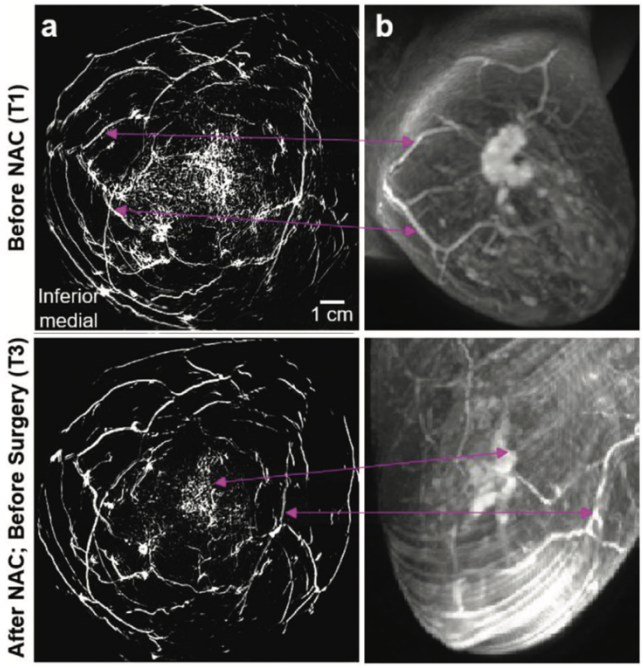

Figure 22. Human breast images acquired using PACT (a) and dynamic contrast enhanced magnetic resonance imagery (DCE-MRI) (b) before and after neoadjuvant chemotherapy. Reproduced with permission from reference [66] (Wiley-VCH GmbH) under Creative Commons CCBY license

Compared to conventional imaging techniques, PACT offers several advantages. Firstly, it provides high-resolution anatomical images, allowing precise localization and characterization of tumors. Secondly, PACT enables the visualization of tumor vascularity, providing valuable information on the tumor's blood supply and response to treatment. Lastly, the fact that PACT can also assess tumor oxygenation levels is a crucial factor influencing treatment outcomes.

PA spectroscopy has also been involved in the study of the cage escape process with notably the contribution of Farid, Gould and coworkers.[9w] Their work reported on the realm of electron-transfer reactions, specifically focusing on their occurrence within the Marcus inverted region. By studying the cyanoanthracene radical anions and alkylbenzene radical cations, they contrasted two types of electron-transfer reactions occurring in the Marcus inverted region: normal charge recombination and charge shift reactions. Charge recombination involves the return of an electron and a positive ion back to their initial states, releasing energy. On the other hand, charge shift reactions entail an overall conservation of charge from the electron moving to a nearby molecule, leading to energy redistribution. The utilization of PA spectroscopy in this study offered a unique perspective on these electron-transfer processes. Analyzing the acoustic signals generated during the reactions allowed to gain a deeper understanding of the energy changes and molecular dynamics involved. Data for calculating the separation quantum yield (k_{et}/k_{sep}) for the system were determined by using both the transient absorption[67] and PA methods which gave very similar results.

Two distinct pathways were considered: (i) charge recombination between cyanoanthracene radical anions and alkylbenzene radical cations and (ii) charge shift reactions between methylacridinium radicals and alkylbenzene radical cations. PA spectroscopy played a pivotal role in obtaining these insights by providing a unique way to monitor the energy changes during these reactions.

In summary, photoacoustic spectroscopy is a powerful technique that combines laser technology and spectroscopy to investigate the absorption characteristics of samples. It has diverse applications and offers advantages such as high sensitivity and versatility. However, careful experimental design and data analysis are crucial to overcome the associated challenges and obtain accurate and meaningful results.

10. Time Resolved Raman Spectroscopy

10.1. Technique overview

The Raman effect is based on the inelastic scattering of light occurring when photons interact with the vibrational modes of molecules. During Raman spectroscopy, most of the scattered light retains the same energy as the incident light (known as Rayleigh scattering), while a small fraction undergoes a change in energy (known as Raman scattering). The analysis of this energy change allows to gain valuable information about the vibrational modes, chemical bonds, and overall molecular structure of the molecules in the sample.[68] Raman spectroscopy has been widely used in various scientific and technological fields, including chemistry, materials science, pharmaceuticals, but also in forensic analysis.[69]

Time-resolved Raman spectroscopy (TRRS) is a specialized technique that provides valuable information about the temporal evolution of molecular vibrations and structural changes in a sample following an external excitation, such as a laser pulse or a photochemical reaction. The principle of TRRS is based on the measurement of Raman spectra as a function of time. It involves the use of short laser pulses to initiate an ultrafast event in the sample, followed by the detection of the Raman-scattered light at various time delays after the excitation (typically ns to fs

timescale). By capturing the temporal evolution of the Raman spectra, it becomes possible to study the dynamics of chemical reactions, molecular rearrangements, and other transient phenomena. The time resolution of TRRS is crucial for capturing fast processes. It relies on specialized techniques such as ultrafast lasers, nonlinear optics, and fast detection systems. The time delay between the pump and probe pulses can be precisely controlled using delay lines or optical delay stages, allowing for the investigation of dynamics on various timescales.[70]

The experimental setup for TRRS typically involves a pump-probe configuration. As depicted in **Figure 23**, a pump laser pulse is used to excite the sample, inducing changes in its molecular structure or vibrational modes. The pump pulse can be tuned to a specific wavelength to target a particular transition or excitation energy. After a controlled time-delay, a laser pulse produced by a Raman laser is employed to probe the sample and collect the Raman-scattered light. The scattered light is then analyzed using a spectrometer and a detector to obtain the Raman spectra at different time points.[71]

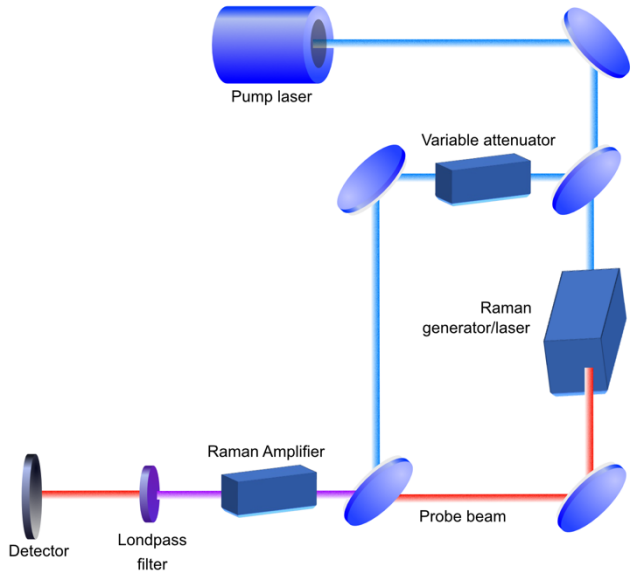

Figure 23. Time resolved Raman spectroscopy setup using the pump-probe technique.

TRRS has been applied to study a wide range of dynamic processes in different fields. In chemistry, it can be used to investigate photochemical reactions, molecular photophysics, and energy transfer processes.[72] In materials science, it enables the study of ultrafast structural changes in materials, including phase transitions, charge transfer, and lattice dynamics.[73] It is also employed in biological research to explore protein folding, enzymatic reactions and DNA dynamics.[74]

One of the major advantages of Raman spectroscopy is its non-destructive nature, as it requires minimal sample preparation. It can analyze samples in various states (solid, liquid, or gas) and can even perform in situ and real-time measurements. Raman spectroscopy also offers high chemical specificity, allowing for the identification and differentiation of closely related compounds.

However, there are certain challenges associated with Raman spectroscopy. One challenge is fluorescence interference, where the sample or impurities fluoresce under laser excitation, overwhelming the Raman signal. This can be addressed by using appropriate laser wavelengths and avoiding fluorescence-prone samples. Another challenge is the relatively weak Raman scattering signal, which requires sensitive detectors and long acquisition times to enhance the signal-to-noise ratio. Additionally, Raman spectroscopy may not be suitable for samples with high water content or strong light absorption.

The analysis of TRRS spectra requires advanced data processing techniques to extract meaningful information from the time-resolved measurements. Kinetic models, spectral fitting algorithms, and multivariate analysis methods are often employed to analyze the time-dependent Raman data and extract kinetic parameters or identify transient species.[70]

10.2. Selected examples from the literature

A study reported in 2019 by Ma, Xhang and Phillips highlights the specific contributions and significance of the application of TRRS in complementarity with transient absorption spectroscopy in the study of water-assisted photoredox reactions of specific aromatic carbonyl compounds.[75] The studied photoreactions are quite unusual and correspond to efficient self-reactions of selected benzophenone derivatives (BPs) and anthraquinone derivatives (AQs) (**Figure 24**) in water as previously reported by Wan and co-workers.[76] In these reactions, the carbonyl functions are reduced to the corresponding phenol meanwhile an alcohol function on a side chain in *meta* position is oxidized to the corresponding ketone. [48-49] The study of Ma, Xhang and Phillips aimed at elucidating the photoredox reaction mechanisms inherent to these categories of BPs and AQs within aqueous environments. A synergistic approach involving femtosecond transient absorption, nanosecond transient absorption, and nanosecond TRRS enabled the detection and comprehensive characterization of both electronic absorption and vibrational spectra of the transient species and intermediates. Functional theory calculations were employed to replicate the electronic absorption and Raman spectra.

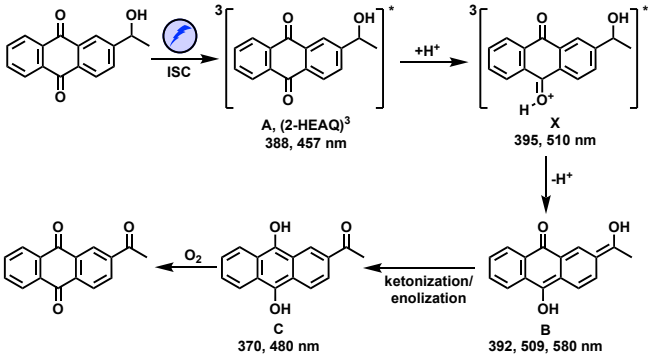

Figure 24. Proposed mechanism of the photoredox reaction of 2-(1-hydroxyethyl)-9,10-anthraquinone (2-HEAQ) under aqueous conditions as determined thanks to fs-TA, ns-TA, and TRRS experiments.[75]

TRRS allowed the investigation of molecular changes and reaction dynamics in real-time to observe and characterize the intermediates and products formed during those specific reactions. **Figure 24** depicts the proposed mechanism for the photoredox reaction of 2-(1-hydroxyethyl)-9,10-anthraquinone (2-HEAQ) under aqueous conditions as determined by femtosecond and nanosecond transient absorption spectroscopy and TRRS

experiments. The proposed mechanism involves an intersystem crossing process following the absorption of light leading to the formation of the triplet excited compound **A, (2-HEAQ)**^{3}. As suggested by the spectroscopic studies, this compound then undergoes protonation to form the triplet excited oxonium that is quenched via proton loss to form compound **B** that tautomerizes into the ketone **C** which is in turn oxidized by molecular oxygen to restitute the anthraquinone moiety.

One of the key advantages of transient Raman spectroscopy in this study is its ability to probe the involvement of water molecules in the photoredox process. Water proved to play a crucial role as a proton source and hydrogen atom donor in the studied reactions and nanosecond TRRS allowed for the direct observation and characterization of those water-mediated processes, shedding light on the specific interactions and dynamics involved. Furthermore, TRRS provided time-resolved information, allowing researchers to monitor the evolution of species and their vibrational changes over the course of the reactions. This temporal resolution is crucial for understanding the kinetics and dynamics of the water-assisted photoredox reactions, providing valuable insights into reaction rates, intermediates, and the overall reaction mechanism.

In summary, the application of TRRS in the study of water-assisted photoredox reactions of aromatic carbonyl compounds provided detailed chemical insights. It allowed for the identification of intermediates, the characterization of reaction pathways, and the probing of water-mediated processes such as protonation and hydrogen atom transfer. The complementarity of transient Raman spectroscopy with other time-resolved spectroscopic techniques enhances the understanding of the kinetics, mechanisms, and overall reactivity of the photoredox reactions.

In summary, Raman spectroscopy is a versatile technique that provides valuable molecular information about samples. It has diverse applications in various scientific and technological fields and offers advantages such as non-destructiveness, chemical specificity, and the ability to analyze samples in different states. Overcoming challenges such as fluorescence interference and weak signal requires careful experimental design and data analysis techniques.

11. Time Resolved Dielectric Loss Spectroscopy

11.1. Technique overview

Time-resolved dielectric loss spectroscopy (TRDL) is typically used to study the dynamic behavior of dielectric materials or small molecules as a function of time. It provides valuable insights into the relaxation processes, charge transport mechanisms, and other time-dependent phenomena occurring in dielectric materials. The principle of TRDL revolves around the measurement of dielectric properties as a function of time after subjecting the material to an external perturbation, such as an electrical pulse or a change in temperature. Dielectric materials respond to these perturbations by undergoing polarization and charge redistribution processes, leading to changes in their dielectric properties.

A typical TRDL setup includes a sample cell containing the dielectric material of interest, electrodes for applying an electric field or measuring capacitance, and a high-speed data acquisition system. The dielectric material is subjected to an external perturbation, such as a step voltage or a temperature change, and the transient response of the material is monitored over time. The time-domain response is then transformed into the frequency domain using Fourier transform to obtain the dielectric loss spectrum.

TRDL spectroscopy finds applications in various fields. In material science, it is commonly used to investigate the relaxation dynamics and charge transport mechanisms in dielectric materials, including polymers and ceramics.[77] The technique is also employed in the study of biological materials, where it provides insights into the dynamics of biomolecules and cellular membranes.[78] Additionally, TRDL is utilized in the characterization of electrical properties in electronic devices and capacitors.[79] The technique has also been recently involved in the characterization of photocatalytic processes occurring in solution and provided mechanistic insights not previously available (*vide infra*).[80]

One of the main advantages of TRDL spectroscopy is its ability to provide information about dynamic processes. It allows for the characterization of relaxation times, charge mobility, and response to time-varying electric fields. The technique is non-destructive and can be used to study both solid and liquid dielectric materials.

However, TRDL spectroscopy also presents some challenges. The experimental setup and data acquisition require high time-resolution capabilities, which can be challenging to achieve. Noise and signal artifacts can affect the accuracy of measurements, necessitating careful calibration and data analysis. Additionally, the interpretation of complex dielectric responses may require the use of sophisticated mathematical models and fitting algorithms.

11.2. Selected examples from the literature

Transition metal complexes are well studied in photocatalysis thanks to their ability to yield long-lived triplet charge transfer states, which can then drive chemical reactions. Most of these complexes being ions, the tailoring of their “inactive” counterions may lead to enhanced photocatalytic reactivity or selectivity. However, solely few studies focused on understanding the dynamic behavior of these counterions in the photoreaction process.[81]

A recent study reported by Early and co-workers relying on TRDL experiments highlights the crucial role of ion-pair reorganization in the regulation of the reactivity of photoredox catalysts.[80] The study focused on photoredox reactions based on the well-known Ir(III) polypyridyl complex $[Ir[dF(CF_3)ppy]_2(dtbpy)]^+X^-$ (Ir[tBu]) that involves charged intermediates. This results in strong interactions with counterions that can significantly influence the reaction outcomes. Indeed, ion-pair reorganization, which refers to the rearrangement of ion pairs during the reaction, affects the stability, solubility, and reactivity of the catalyst and its associated intermediates.

TRDL spectroscopy appeared to be a powerful technique that offers a unique tool to investigate the dynamics of ion-pair

reorganization in photoredox catalysts by providing crucial information about the dielectric properties and molecular mobility of the ion pairs, allowing for a direct probe into their structural changes and relaxation processes.

In this study, TRDL showed the impact of the counter-ion structure on the excited-state charge distribution which proved to lead to major changes in both the ground- and excited-state dipole moment. This was realized by using either a small associating anion (PF_6^-) that forms a contact-ion pair and a larger one ($BArF_4^-$) that can either dissociate or form a solvent-separated pair. These differences were revealed by TRDL experiments with the negative change in the imaginary permittivity (ε'') indicating that the excited-state dipole moment is smaller in the excited state than in the ground state, providing evidence of contact-ion pair reorganization. Conversely, the positive change in imaginary permittivity observed for Ir[tBu]–$BArF_4$ likely arose from an increase in the intramolecular dipole moment in the excited MLCT state. This was observed due to the absence of contact-ion pairing between $BArF_4$ and the Ir[tBu] complex.

These inherent differences were found to have a correlation with the photocatalyst's reactivity in terms of both reductive and oxidative electron transfer. Indeed, for the reducing agents (4-methoxytriphenylamine, tris(4-bromophenyl)amine, and 1,4-dimethoxybenzene), altering the anion from PF_6^- to $BArF_4^-$ resulted in an approximately 2-fold increase in the rate constant of electron transfer. Conversely, for the oxidative agents (4-nitrobenzonitrile, 4-chloronitrobenzene, phthalic anhydride), transitioning from PF_6^- to $BArF_4^-$ led to an approximately 0.5-fold decrease in the electron transfer rate constant. This corresponds to a 4-fold shift in substrate oxidation selectivity when X− is $BArF_4^-$ instead of PF_6^-. From these electron transfer kinetics, it is obvious that the choice of counter-ion can impact the overall effectiveness of the photocatalyst. Furthermore, these findings align qualitatively with prior studies on other cationic photoredox catalysts, suggesting that the anion's role can be critical.[81-82]

Besides ion-pair dynamics, the TRDL data also allowed to propose the evolution of the Ir[tBu]-PF_6 state which is presented in **Figure 25**. The ascertained dipole moment of the relaxed MLCT state within $[Ir[dF(CF_3)ppy]_2(dtbpy)]^+X^-$ substantially deviated from the predictions of simplistic point-charge computations. This deviation, coupled with a limited polarizability volume, signified a predominantly confined end state characterized by mixed metal-ligand attributes. This contrasts with the initial MLCT states of high polarizability observed within the timescale of the instrument's response.

The figure displays the intramolecular dipole moment in purple, the intermolecular dipole moment in yellow and the overall vector-sum dipole moment observed using TRDL in green. The dipole moment measured in state A (**Figure 23**, pink) represent an average of two resonance structures. These revelations were enabled using computational methodologies, rejuvenating TRDL spectroscopy as a foundational instrument for investigating the electronic configuration of molecules in both their ground and excited states within a solution. Electromagnetic simulations of the microwave cavity's response function and the computation of the molecular dipolar relaxation time collectively enhance the precision and extensive applicability of TRDL spectroscopy.

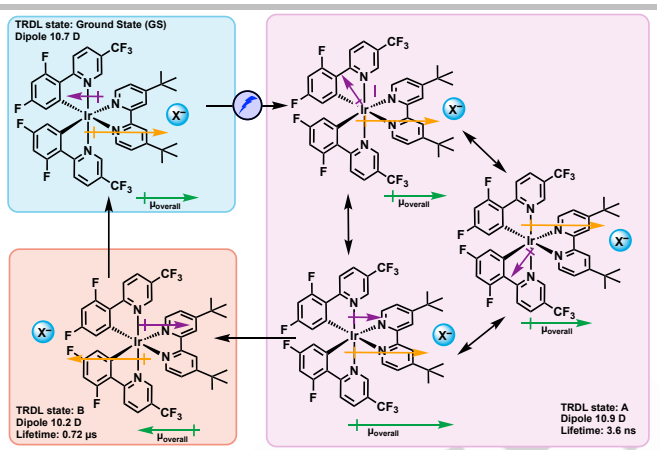

Figure 25. Proposed Ir[tBu]-PF6 state evolution from TRDL data.[80] The intramolecular (purple), intermolecular (orange) and overall vector-sum (green) dipole moment observed by TRDL. In State A (right), the dipole moment is an average of the two resonance structures.

In summary, the study emphasized the significance of ion-pair reorganization in governing the reactivity of photoredox catalysts. The investigation of ion-pair dynamics using advanced spectroscopic techniques can help providing mechanistic insights, revealing the influence of solvents, and offering molecular design strategies for optimizing catalyst performance. Understanding and controlling ion-pair reorganization is crucial for advancing the field of photoredox catalysis and developing efficient and selective transformations.

In most of the literature reports, TRDL is often used in combination with other spectroscopic techniques such as transient absorption spectroscopy, time resolved infrared spectroscopy and pulse radiolysis. While these techniques provide insights into electronic and vibrational transitions, TRDL focuses on the collective behavior of the ion pairs and their interaction with the surrounding solvent environment.[42b]

Time-resolved dielectric loss spectroscopy also provides solvent-specific information regarding the ion-pair dynamics. Different solvents exhibit varying dielectric properties, which influence the stability and mobility of ion pairs. By utilizing this technique, solvent-dependent effects on ion-pair equilibria can be investigated and better understanding of how solvent choice affects the catalyst's reactivity can be made. This allows to optimize reaction conditions and solvent selection.

12. Summary and Future Outlook

Within this concept article, we gathered a selection of spectroscopic techniques that are used, or could be used, for mechanistic investigations of light-induced reactions. We aimed at providing a different perspective on mechanistic photoredox catalysis than the currently available library of reviews relative to that topic. Most of the techniques reported herein offer powerful tools to investigate the behavior and reactivity of reaction intermediates with several techniques that provide direct observation of key intermediates, electronic structure characterization, kinetic analysis, and mechanistic insights, all of

which contribute to the advancement of catalysis and the development of more efficient synthetic methodologies.

Taking **Figure 1** as inspiration, we believe that the following aspects will undoubtedly (continue to) be investigated and optimized in the future.

- **Development of novel photosensitizers.** Prototypical Ru(II) and Ir(III) photosensitizers represent the warhead of photoredox catalysis, yet the low abundance of these elements limits their widespread use, unless specific recycling efforts are realized (*vide infra*). There is therefore a need for the development of photosensitizers that are based on earth abundant metals, that are also responsibly sourced. Cobalt, for example, is relatively abundant but is sourced from extensive mining, mainly in the democratic republic of Congo, that comes with both human and environmental concerns. Therefore, efforts to develop novel photosensitizers based on earth abundant photosensitizers are highly sought after and several groups have already pioneered their use. This allows to develop new classes of photosensitizers that could hopefully one day, substitute prototypical Ru(II) and Ir(III) photosensitizers.
- **Novel mechanistic pathways and photon up-conversion**. Several investigations are currently focused on the use of less energetic red light to drive organic reactions. In theory, this limits the scope of activatable substrates but would allow to make better use of the large number of red photons that come from the sun, if the sun were to be used as light source. There are already reports that used Os(II) complexes[83] or polynuclear Ru(II) complexes[84] to drive photoredox transformations using orange-red light irradiation. An approach using a Cu(I) photosensitizer and a dicyanoanthracene organic photosensitizer was recently investigated as a red-light based dual photoredox system.[85] As such, the Cu(I) photosensitizer was excited with red light which led to the excited-state reduction of dicyanoanthracene, whose corresponding radical anion also absorbed red light to perform challenging reactions. Photon upconversion *via* triplet-triplet annihilation also represents a promising avenue that will take advantage of red-light absorbing chromophore to activate blue or UV emitter for substrate photo-activation.[13, 17n, 86]
- **Mechanistic investigations.** As the main topic of this concept article, we firmly believe that mechanistic investigations will continue to thrive and that novel or underexplored spectroscopic techniques will provide valuable information. This is where Ru(II) and Ir(III) photosensitizers in particular will continue to thrive as they are generally robust under irradiation and will allow to develop novel reaction scopes that can be studies into details using the above-mentioned spectroscopic techniques. This will then provide key design principle that can be tested and adapted to the next generation of earth abundant photosensitizers that is currently being prepared in several pioneering laboratories and emerging ones.
- **Recyclability.** For the field to further being credible in proposing a sustainable approach towards chemistry using sunlight as photon source, it is necessary to tackle and address the recyclability issues of certain photosensitizers. Some Ru(II) photosensitizers for example are known to populate the ligand field state upon illumination, which can lead to ligand loss and subsequent decomposition of the photosensitizer during the reaction.[84, 87] In addition to destroying the photosensitizer, this can also possibly induce additional side reaction pathways. The lack of investigation of recyclability leads to false report and sometimes false believes. Heteroleptic copper complexes are a prime example of compounds that warrant a deeper investigation into their recyclability.[17b] Their announced photostability in the plethora of photoredox catalysis reactions is dubious as phosphine ligands can also undergo oxidation reaction which would limit their applicability. Heterogenization strategies could help investigate the robustness and recyclability of certain complex, but that approach comes with limitations of their own.[88] The iron photosensitizer reported by Wärnmark et al. shows great promise regarding recyclability as it remained intact and could be easily recovered in 88% yield after the photoreaction.[9b] These photosensitizers still need to show a broader range of substrate activation to fully expand the scope of available transformations.
- **Cage escape yields.** The cage-escape yields, i.e., the efficiency with which the geminate radical pair escapes the solvent cage, was shown to have a drastic influence of the overall reaction yields. The determination of cage-escape yields for several systems was already performed in the 1970's and 1980's but they are currently experiencing a regained interest due to their importance in light-induced transformations. Hence, understanding the factors that play a role in those cage-escape processes is of paramount importance. The experimental protocol (Eq. 4 and 5) that is used to determine ϕ_{CE} is applicable to both reductive and oxidative electron transfer but also suffers from some limitations. For example, the photosensitizer and quencher must remain stable during the experiment. The photosensitizer and actinometer must absorb at the same excitation wavelength for Eq. 4 and 5 to be applicable. Finally, the changes in absorbance between the PS in the ground state and the $PS^{\bullet+}$ or the $PS^{\bullet-}$ must be sufficiently important to accurately determine the $\Delta\varepsilon$ value and measure the corresponding single wavelength absorption changes. As such, nanosecond transient absorption spectroscopy is key to determining those yields, but other techniques will most probably be used for such measurements. This will bring a deeper understanding into the cage-escape processes and lead to more optimized photosensitized chemical transformations.

Acknowledgements

L.T.-G. is a Chercheur Qualifié of the Fonds de la Recherche Scientifique – FNRS. S.D.K., M.G., B.E. and L.T.-G. gratefully acknowledge the UCLouvain for financial support. This work was supported by the Fonds de la Recherche Scientifique (F.R.S.-FNRS) under grant no. U.N021.21 (B.E.)

Keywords: Photoredox Catalysis • Spectroscopy • Electron Transfer • Energy Transfer • Cage-Escape

References

1

[1] D. M. Chapin, C. S. Fuller and G. L. Pearson, *Journal of Applied Physics* **1954**, *25*, 676-677.

[2] a) B. Zhang and L. Sun, *Chem. Soc. Rev.* **2019**, *48*, 2216-2264; b) D. G. Nocera, *Acc. Chem. Res.* **2012**, *45*, 767-776; c) T. J. Meyer, *Acc. Chem. Res.* **1989**, *22*, 163-170; d) D. Gust, T. A. Moore and A. L. Moore, *Theor. Exp. Plant. Phys.* **2013**, *25*, 182-185; e) D. Gust, T. A. Moore and A. L. Moore, *Acc. Chem. Res.* **2009**, *42*, 1890-1898; f) J. J. Concepcion, R. L. House, J. M. Papanikolas and T. J. Meyer, *Proc. Natl. Acad. Sci. USA* **2012**, *109*, 15560-15564; g) V. Balzani, A. Credi, F. M. Raymo and J. F. Stoddart, *Angew. Chem. Int. Ed.* **2000**, *39*, 3348-3391; h) V. Balzani, A. Credi, B. Ferrer, S. Silvi and M. Venturi in *Artificial Molecular Motors and Machines: Design Principles and Prototype Systems*, (Ed. T. R. Kelly), Springer Berlin Heidelberg, Berlin, Heidelberg, **2005**, pp. 1-27; i) E. S. Andreiadis, M. Chavarot-Kerlidou, M. Fontecave and V. Artero, *Photochem. Photobiol.* **2011**, *87*, 946-964.

[3] G. Ciamician and P. Silber, *Ber. Dtsch. Chem. Ges.* **1908**, *41*, 1071-1080.

[4] M. Marchini, G. Bergamini, P. G. Cozzi, P. Ceroni and V. Balzani, *Angew. Chem. Int. Ed.* **2017**, *56*, 12820-12821.

[5] O. Stern and M. Volmer, *Physik Z.* **1919**, *20*, 183-188.

[6] a) L. Troian-Gautier, M. D. Turlington, S. A. M. Wehlin, A. B. Maurer, M. D. Brady, W. B. Swords and G. J. Meyer, *Chem. Rev.* **2019**, *119*, 4628-4683; b) A. Marton, C. C. Clark, R. Srinivasan, R. E. Freundlich, A. A. Narducci Sarjeant and G. J. Meyer, *Inorg. Chem.* **2006**, *45*, 362-369; c) C. C. Clark, A. Marton and G. J. Meyer, *Inorg. Chem.* **2005**, *44*, 3383-3385; d) B. H. Farnum, J. M. Gardner, A. Marton, A. A. Narducci-Sarjeant and G. J. Meyer, *Dalton Trans.* **2011**, *40*, 3830-3838.

[7] D. Genovese, M. Cingolani, E. Rampazzo, L. Prodi and N. Zaccheroni, *Chem. Soc. Rev.* **2021**, *50*, 8414-8427.

[8] a) R. A. Marcus, *Reviews of Modern Physics* **1993**, *65*, 599-610; b) E. J. Piechota and G. J. Meyer, *J. Chem. Ed.* **2019**, *96*, 2450-2466.

[9] a) A. Aydogan, R. E. Bangle, S. De Kreijger, J. C. Dickenson, M. L. Singleton, E. Cauët, A. Cadranel, G. J. Meyer, B. Elias, R. N. Sampaio and L. Troian-Gautier, *Catal. Sci. Technol.* **2021**, *11*, 8037-8051; b) A. Aydogan, R. E. Bangle, A. Cadranel, M. D. Turlington, D. T. Conroy, E. Cauët, M. L. Singleton, G. J. Meyer, R. N. Sampaio, B. Elias and L. Troian-Gautier, *J. Am. Chem. Soc.* **2021**, *143*, 15661-15673; c) A. Ripak, S. De Kreijger, R. N. Sampaio, C. A. Vincent, É. Cauët, I. Jabin, U. K. Tambar, B. Elias and L. Troian-Gautier, *Chem Catal.* **2023**, 100490; d) J. Olmsted and T. J. Meyer, *J. Phys. Chem* **1987**, *91*, 1649-1655; e) T. H. Bürgin, F. Glaser and O. S. Wenger, *Journal of the American Chemical Society* **2022**, *144*, 14181-14194; f) B. Shan and R. Schmehl, *J. Phys. Chem. A* **2014**, *118*, 10400-10406; g) L. Troian-Gautier, E. E. Beauvilliers, W. B. Swords and G. J. Meyer, *J. Am. Chem. Soc.* **2016**, *138*, 16815-16826; h) H.-J. Wolff, D. Burssher and U. E. Steiner, *Pure Appl. Chem.* **1995**, *67*, 167-174; i) A. B. Stickrath, E. C. Carroll, X. Dai, D. A. Harris, A. Rury, B. Smith, K.-C. Tang, J. Wert and R. J. Sension, *J. Phys. Chem. A* **2009**, *113*, 8513-8522; j) U. E. Steiner and D. Bürßner, *Z. Phys. Chem.* **1990**, *169*, 159-180; k) N. Periasamy and H. Linschitz, *Chem. Phys. Lett.* **1979**, *64*, 281-285; l) K. Oppelt, R. Fernández-Terán, R. Pfister and P. Hamm, *J. Phys. Chem. C* **2019**, *123*, 19952-19961; m) A. B. Oelkers, L. F. Scatena and D. R. Tyler, *J. Phys. Chem. A* **2007**, *111*, 5353-5360; n) L. A. Lucia and K. S. Schanze, *Inorg. Chim. Acta* **1994**, *225*, 41-49; o) K. Kalyanasundaram and M. Neumann-Spallart, *Chem. Phys. Lett.* **1982**, *88*, 7-12; p) M. Z. Hoffman, *J. Phys. Chem* **1988**, *92*, 3458-3464; q) M. Georgopoulos and M. Z. Hoffman, *J. Phys. Chem* **1991**, *95*, 7717-7721; r) C. Chiorboli, M. T. Indelli, M. A. Rampi Scandola and F. Scandola, *J. Phys. Chem* **1988**, *92*, 156-163; s) U. Bhattacharjee, C. A. Chesta and R. G. Weiss, *Photochem. Photobio. Sci.* **2004**, *3*, 287-295; t) R. E. Adams and R. H. Schmehl, *Langmuir* **2016**, *32*, 8598-8607; u) F. D. Lewis, R. E. Dykstra, I. R. Gould and S. Farid, *J. Phys. Chem* **1988**, *92*, 7042-7043; v) F. D. Lewis, A. M. Bedell, R. E. Dykstra, J. E. Elbert, I. R. Gould and S. Farid, *J. Am. Chem. Soc.* **1990**, *112*, 8055-8064; w) I. R. Gould, R. Moody and S. Farid, *J. Am. Chem. Soc.* **1988**, *110*, 7242-7244; x) S. S. Jayanthi and P. Ramamurthy, *Phys. Chem. Chem. Phys.* **1999**, *1*, 4751-4757; y) K. S. Kjær, N. Kaul, O. Prakash, P. Chábera, N. W. Rosemann, A. Honarfar, O. Gordivska, L. A. Fredin, K.-E. Bergquist, L. Häggström, T. Ericsson, L. Lindh, A. Yartsev, S. Styring, P. Huang, J. Uhlig, J. Bendix, D. Strand, V. Sundström, P. Persson, R. Lomoth and K. Wärnmark, *Science* **2019**, *363*, 249-253; z) N. W. Rosemann, P. Chábera, O. Prakash, S. Kaufhold, K. Wärnmark, A. Yartsev and P. Persson, *J. Am. Chem. Soc.* **2020**, *142*, 8565-8569; aa) A. Ilic, J. Schwarz, C. Johnson, L. H. M. de Groot, S. Kaufhold, R. Lomoth and K. Wärnmark, *Chem. Sci.* **2022**, *13*, 9165-9175; ab) J. Schwarz, A. Ilic, C. Johnson, R. Lomoth and K. Wärnmark, *Chem. Commun.* **2022**, *58*, 5351-5354; ac) H. Masuhara and N. Mataga, *Acc. Chem. Res.* **1981**, *14*, 312-318; ad) M. S. Coles, G. Quach, J. E. Beves and E. G. Moore, *Angew. Chem. Int. Ed.* **2020**, *59*, 9522-9526; ae) K. Miedlar and P. K. Das, *J. Am. Chem. Soc.* **1982**, *104*, 7462-7469; af) G. Neshvad and M. Z. Hoffman, *J. Phys. Chem* **1989**, *93*, 2445-2452; ag) A. Senz and H. E. Gsponer, *J. Phys. Org. Chem.* **1995**, *8*, 706-712; ah) S. Neumann, O. S. Wenger and C. Kerzig, *Chem-Eur. J.* **2021**, *27*, 4115-4123; ai) S. Sittel, A. C. Sell, K. Hofmann, C. Wiedemann, J. P. Nau, C. Kerzig, G. Manolikakes and K. Heinze, *ChemCatChem* **2023**, *15*, e202201562; aj) A. Ripak, S. De Kreijger, B. Elias and L. Troian-Gautier, *STAR Protocols* **2023**, *4*, 102312.

[10] A. Ripak, S. De Kreijger, R. N. Sampaio, C. A. Vincent, É. Cauët, I. Jabin, U. K. Tambar, B. Elias and L. Troian-Gautier, *Chem Catalysis* **2023**, *3*, 100490.

[11] D. A. Kurtz and J. L. Dempsey, *Inorg. Chem.* **2019**, *58*, 16510-16517.

[12] a) B. N. DiMarco, R. M. O'Donnell and G. J. Meyer, *J. Phys. Chem. C* **2015**, *119*, 21599-21604; b) S. A. M. Wehlin, L. Troian-Gautier, G. Li and G. J. Meyer, *J. Am. Chem. Soc.* **2017**, *139*, 12903-12906.

[13] F. Glaser, C. Kerzig and O. S. Wenger, *Chem. Sci.* **2021**, *12*, 9922-9933.

[14] a) A. Cadranel, G. E. Pieslinger, P. Tongying, M. K. Kuno, L. M. Baraldo and J. H. Hodak, *Dalton Trans.* **2016**, *45*, 5464-5475; b) A. Cadranel and J. H. Hodak, *J. Coord. Chem.* **2015**, *68*, 1452-1464; c) A. Cotic, S. Cerfontaine, L. D. Slep, B. Elias, L. Troian-Gautier and A. Cadranel, *J. Am. Chem. Soc.* **2023**, *145*, 5163-5173; d) A. Cotic, S. Cerfontaine, L. D. Slep, B. Elias, L. Troian-Gautier and A. Cadranel, *Phys. Chem. Chem. Phys.* **2022**, *24*, 15121-15128; e) L. Suntrup, F. Stein, G. Hermann, M. Kleoff, M. Kuss-Petermann, J. Klein, O. S. Wenger, J. C. Tremblay and B. Sarkar, *Inorg. Chem.* **2018**, *57*, 13973-13984; f) P. Chábera, Y. Liu, O. Prakash, E. Thyrhaug, A. E. Nahhas, A. Honarfar, S. Essén, L. A. Fredin, T. C. B. Harlang, K. S. Kjær, K. Handrup, F. Ericson, H. Tatsuno, K. Morgan, J. Schnadt, L. Häggström, T. Ericsson, A. Sobkowiak, S. Lidin, P. Huang, S. Styring, J. Uhlig, J. Bendix, R. Lomoth, V. Sundström, P. Persson and K. Wärnmark, *Nature* **2017**, *543*, 695-699; g) O. Prakash, L. Lindh, N. Kaul, N. W. Rosemann, I. B. Losada, C. Johnson, P. Chábera, A. Ilic, J. Schwarz, A. K. Gupta, J. Uhlig, T. Ericsson, L. Häggström, P. Huang, J. Bendix, D. Strand, A. Yartsev, R. Lomoth, P. Persson and K. Wärnmark, *Inorg. Chem.* **2022**, *61*, 17515-17526; h) R. N. Sampaio, E. J. Piechota, L. Troian-Gautier, A. B. Maurer, K. Hu, P. A. Schauer, A. D. Blair, C. P. Berlinguette and G. J. Meyer, *Proc. Natl. Acad. Sci. USA* **2018**, *115*, 7248-7253; i) R. N. Sampaio, L. Troian-Gautier and G. J. Meyer, *Angew. Chem.* **2018**, *130*, 15616-15620; j) E. J. Piechota, R. N. Sampaio, L. Troian-Gautier, A. B. Maurer, C. P. Berlinguette and G. J. Meyer, *J. Phys. Chem. C* **2019**, *123*, 3416-3425; k) D. Wang, R. N. Sampaio, L. Troian-Gautier, S. L. Marquard, B. H. Farnum, B. D. Sherman, M. V. Sheridan, C. J. Dares, G. J. Meyer and T. J. Meyer, *J. Am. Chem. Soc.* **2019**, *141*, 7926-7933; l) R. Holze, *Journal of Solid State Electrochemistry* **2004**, *8*, 982-997; m) W. Kaim, B. Sarkar and G. Kumar

Lahiri in *Mixed-Valence Intermediates as Ideal Targets for Spectroelectrochemistry (SEC)*, Eds.: W. Kaim and A. Klein), The Royal Society of Chemistry, **2008**, p. 0; n) S. Dhungana and A. L. Crumbliss in *UV-Vis Spectroelectrochemistry of Selected Iron-Containing Proteins*, Eds.: W. Kaim and A. Klein), The Royal Society of Chemistry, **2008**, p. 0; o) S. P. Best, S. J. Borg and K. A. Vincent in *Infrared Spectroelectrochemistry*, Eds.: W. Kaim and A. Klein), The Royal Society of Chemistry, **2008**, p. 0; p) J. Catherine Salsman and C. P. Kubiak in *Infrared Spectroelectrochemical Investigations of Ultrafast Electron Transfer in Mixed-Valence Complexes*, Eds.: W. Kaim and A. Klein), The Royal Society of Chemistry, **2008**, p. 0; q) P. R. Murray and L. J. Yellowlees in *EPR Spectroelectrochemistry*, Eds.: W. Kaim and A. Klein), The Royal Society of Chemistry, **2008**, p. 0.

[15] E. J. Piechota, L. Troian-Gautier, R. N. Sampaio, M. K. Brennaman, K. Hu, C. P. Berlinguette and G. J. Meyer, *J. Am. Chem. Soc.* **2018**, *140*, 7176-7186.

[16] a) W. B. Swords and T. P. Yoon in *Transient absorption spectroscopy in visible-light photocatalysis*, *Vol. 50* Eds.: S. Crespi and S. Protti), The Royal Society of Chemistry, **2022**, p. 0; b) R. G. W. Norrish and G. Porter, *Nature* **1949**, *164*, 658-658; c) G.-N. Porter and R. G. W. Norrish, *Proceedings of the Royal Society of London. Series A. Mathematical and Physical Sciences* **1950**, *200*, 284-300; d) G. Porter, *Science* **1968**, *160*, 1299-1307; e) M. Eigen, G. Kurtze and K. Tamm, *Zeitschrift für Elektrochemie, Berichte der Bunsengesellschaft für physikalische Chemie* **1953**, *57*, 103-118; f) M. Eigen, *Z. Phys. Chem.* **1954**, *1*, 176-200.

[17] a) L. Liu, T. Duchanois, T. Etienne, A. Monari, M. Beley, X. Assfeld, S. Haacke and P. C. Gros, *Phys. Chem. Chem. Phys.* **2016**, *18*, 12550-12556; b) J. Beaudelot, S. Oger, S. Peruško, T.-A. Phan, T. Teunens, C. Moucheron and G. Evano, *Chem. Rev.* **2022**, *122*, 16365-16609; c) S. Engl and O. Reiser, *Eur. J. Org. Chem.* **2020**, *2020*, 1523-1533; d) M. C. Rosko, K. A. Wells, C. E. Hauke and F. N. Castellano, *Inorg. Chem.* **2021**, *60*, 8394-8403; e) M. Yang, S. Sheykhi, Y. Zhang, C. Milsmann and F. N. Castellano, *Chem. Sci.* **2021**, *12*, 9069-9077; f) Y. Liu, T. Harlang, S. E. Canton, P. Chábera, K. Suárez-Alcántara, A. Fleckhaus, D. A. Vithanage, E. Göransson, A. Corani, R. Lomoth, V. Sundström and K. Wärnmark, *Chem. Commun.* **2013**, *49*, 6412-6414; g) S. Otto, M. Grabolle, C. Förster, C. Kreitner, U. Resch-Genger and K. Heinze, *Angew. Chem. Int. Ed.* **2015**, *54*, 11572-11576; h) L. A. Büldt, X. Guo, R. Vogel, A. Prescimone and O. S. Wenger, *J. Am. Chem. Soc.* **2017**, *139*, 985-992; i) T. C. B. Harlang, Y. Liu, O. Gordivska, L. A. Fredin, C. S. Ponseca, P. Huang, P. Chábera, K. S. Kjaer, H. Mateos, J. Uhlig, R. Lomoth, R. Wallenberg, S. Styring, P. Persson, V. Sundström and K. Wärnmark, *Nature Chemistry* **2015**, *7*, 883-889; j) D. G. Cuttell, S.-M. Kuang, P. E. Fanwick, D. R. McMillin and R. A. Walton, *J. Am. Chem. Soc.* **2002**, *124*, 6-7; k) Y. Zhang, J. L. Petersen and C. Milsmann, *J. Am. Chem. Soc.* **2016**, *138*, 13115-13118; l) Y. Zhang, T. S. Lee, J. L. Petersen and C. Milsmann, *J. Am. Chem. Soc.* **2018**, *140*, 5934-5947; m) L. A. Büldt, X. Guo, A. Prescimone and O. S. Wenger, *Angew. Chem. Int. Ed.* **2016**, *55*, 11247-11250; n) W. R. Kitzmann, M.-S. Bertrams, P. Boden, A. C. Fischer, R. Klauer, J. Sutter, R. Naumann, C. Förster, G. Niedner-Schatteburg, N. H. Bings, J. Hunger, C. Kerzig and K. Heinze, *J. Am. Chem. Soc.* **2023**, *145*, 16597-16609; o) C. Wang, F. Reichenauer, W. R. Kitzmann, C. Kerzig, K. Heinze and U. Resch-Genger, *Angew. Chem. Int. Ed.* **2022**, *61*, e202202238.

[18] D. W. Thompson, A. Ito and T. J. Meyer, *Pure Appl. Chem.* **2013**, *85*, 1257-1305.

[19] a) J. C. Deaton and F. N. Castellano in *Archetypal Iridium(III) Compounds for Optoelectronic and Photonic Applications*, (Ed. E. Zysman-Colman), John Wiley & Sons Ltc., Chichester, West Sussex, **2017**, pp. 1-69; b) R. Bevernaegie, S. A. M. Wehlin, B. Elias and L. Troian-Gautier, *ChemPhotoChem* **2021**, *5*, 217-234; c) R. Bevernaegie, S. A. M. Wehlin, E. J. Piechota, M. Abraham, C. Philouze, G. J. Meyer, B. Elias and L. Troian-Gautier, *J. Am. Chem. Soc.* **2020**, *142*, 2732-2737; d) C. M. Morton, Q. Zhu, H. Ripberger, L. Troian-Gautier, Z. S. D. Toa, R. R. Knowles and E. J. Alexanian, *J. Am. Chem. Soc.* **2019**, *141*, 13253-13260; e) B. Xu, L. Troian-Gautier, R. Dykstra, R. T. Martin, O. Gutierrez and U. K. Tambar, *J. Am. Chem. Soc.* **2020**, *142*, 6206-6215.

[20] I. Ghosh, R. S. Shaikh and B. König, *Angew. Chem. Int. Ed.* **2017**, *56*, 8544-8549.

[21] C. R. Bock, T. J. Meyer and D. G. Whitten, *J. Am. Chem. Soc.* **1975**, *97*, 2909-2911.

[22] I. Ghosh, J. I. Bardagi and B. König, *Angew. Chem. Int. Ed.* **2017**, *56*, 12822-12824.

[23] B. G. Stevenson, E. H. Spielvogel, E. A. Loiaconi, V. M. Wambua, R. V. Nakhamiyayev and J. R. Swierk, *J. Am. Chem. Soc.* **2021**, *143*, 8878-8885.

[24] a) A. van den Bosch, D. Stienlet and J. Ceulemans, *Radiat. Phys. Chem. Int. J. Radiat. Appl. Instrum., Part C* **1989**, *33*, 371-379; b) T. Ichikawa and N. Ota, *J. Phys. Chem* **1987**, *91*, 3244-3248.

[25] A. Olaya-Castro and G. D. Scholes, *International Reviews in Physical Chemistry* **2011**, *30*, 49-77.

[26] E. R. Welin, C. Le, D. M. Arias-Rotondo, J. K. McCusker and D. W. C. MacMillan, *Science* **2017**, *355*, 380-385.

[27] L. Tian, N. A. Till, B. Kudisch, D. W. C. MacMillan and G. D. Scholes, *J. Am. Chem. Soc.* **2020**, *142*, 4555-4559.

[28] C. Ruckebusch, M. Sliwa, P. Pernot, A. de Juan and R. Tauler, *J. Photoch. Photobio. C* **2012**, *13*, 1-27.

[29] B. Elias, C. Creely, G. W. Doorley, M. M. Feeney, C. Moucheron, A. Kirsch-DeMesmaeker, J. Dyer, D. C. Grills, M. W. George, P. Matousek, A. W. Parker, M. Towrie and J. M. Kelly, *Chem-Eur. J.* **2008**, *14*, 369-375.

[30] J. M. R. Narayanam, J. W. Tucker and C. R. J. Stephenson, *J. Am. Chem. Soc.* **2009**, *131*, 8756-8757.

[31] F. Cao, J. Kim and A. J. Bard, *J. Am. Chem. Soc.* **2014**, *136*, 18163-18169.

[32] L. X. Chen in *X-Ray Transient Absorption Spectroscopy*, **2016**, pp. 213-249.

[33] A. Iglesias-Juez, G. L. Chiarello, G. S. Patience and M. O. Guerrero-Pérez, *The Canadian Journal of Chemical Engineering* **2022**, *100*, 3-22.

[34] a) X. Zhang, S. E. Canton, G. Smolentsev, C.-J. Wallentin, Y. Liu, Q. Kong, K. Attenkofer, A. B. Stickrath, M. W. Mara, L. X. Chen, K. Wärnmark and V. Sundström, *J. Am. Chem. Soc.* **2014**, *136*, 8804-8809; b) L. X. Chen, X. Zhang, E. C. Wasinger, K. Attenkofer, G. Jennings, A. Z. Muresan and J. S. Lindsey, *J. Am. Chem. Soc.* **2007**, *129*, 9616-9618.

[35] J.-W. Wang, X. Zhang, L. Velasco, M. Karnahl, Z. Li, Z.-M. Luo, Y. Huang, J. Yu, W. Hu, X. Zhang, K. Yamauchi, K. Sakai, D. Moonshiram and G. Ouyang, *JACS Au* **2023**, *3*, 1984-1997.

[36] a) Y. Pushkar, D. Moonshiram, V. Purohit, L. Yan and I. Alperovich, *J. Am. Chem. Soc.* **2014**, *136*, 11938-11945; b) C. Gimbert-Suriñach, D. Moonshiram, L. Francàs, N. Planas, V. Bernales, F. Bozoglian, A. Guda, L. Mognon, I. López, M. A. Hoque, L. Gagliardi, C. J. Cramer and A. Llobet, *J. Am. Chem. Soc.* **2016**, *138*, 15291-15294.

[37] a) L. Velasco, C. Liu, X. Zhang, S. Grau, M. Gil-Sepulcre, C. Gimbert-Suriñach, A. Picón, A. Llobet, S. DeBeer and D. Moonshiram, *ChemSusChem* **2023**, *n/a*, e202300719; b) J. Zhao, S. De Kreijger, L. Troian-Gautier, J. Yu, W. Hu, X. Zhang, B. Elias and D. Moonshiram, *Chem. Commun.* **2022**, *58*, 8057-8060; c) Z.-J. Li, F. Zhan, H. Xiao, X. Zhang, Q.-Y. Kong, X.-B. Fan, W.-Q. Liu, M.-Y. Huang, C. Huang, Y.-J. Gao, X.-B. Li, Q.-Y. Meng, K. Feng, B. Chen, C.-H. Tung, H.-F. Zhao, Y. Tao and L.-Z. Wu, *J. Phys. Chem. Lett.* **2016**, *7*, 5253-5258.

[38] G. K. Jayasekara, C. Antolini, M. A. Smith, D. J. Jacoby, J. Escolastico, N. Girard, B. T. Young and D. Hayes, *J. Am. Chem. Soc.* **2021**, *143*, 19356-19364.

[39] D. Moonshiram, C. Gimbert-Suriñach, A. Guda, A. Picon, C. S. Lehmann, X. Zhang, G. Doumy, A. M. March, J. Benet-Buchholz, A. Soldatov, A. Llobet and S. H. Southworth, *J. Am. Chem. Soc.* **2016**, *138*, 10586-10596.

[40] a) S. Varma, C. E. Castillo, T. Stoll, J. Fortage, A. G. Blackman, F. Molton, A. Deronzier and M.-N. Collomb, *Phys. Chem. Chem. Phys.* **2013**, *15*, 17544-17552; b) C. Gimbert-Suriñach, J. Albero, T. Stoll, J. Fortage, M.-N. Collomb, A. Deronzier, E. Palomares and A. Llobet, *J. Am. Chem. Soc.* **2014**, *136*, 7655-7661.

[41] a) V. Artero, M. Chavarot-Kerlidou and M. Fontecave, *Angew. Chem. Int. Ed.* **2011**, *50*, 7238-7266; b) J. L. Dempsey, B. S. Brunschwig, J. R. Winkler and H. B. Gray, *Acc. Chem. Res.* **2009**, *42*, 1995-2004.

[42] a) Y. Jinfeng, K. Koichi, G. Masao and Y. Yoichi in *Femtosecond Pulse Radiolysis*, (Ed. Y. Jinfeng), IntechOpen, Rijeka, **2020**, p. Ch. 3; b) A. Millet, P. T. Cesana, K. Sedillo, M. J. Bird, G. S. Schlau-Cohen, A. G.

Doyle, D. W. C. MacMillan and G. D. Scholes, *Acc Chem Res* **2022**, *55*, 1423-1434; c) L. K. Folkes, S. Bartesaghi, M. Trujillo, P. Wardman and R. Radi, *International Journal of Molecular Sciences* **2022**, *23*, 1797.

[43] a) R. Kissner, T. Nauser, P. Bugnon, P. G. Lye and W. H. Koppenol, *Chem. Res. Toxicol.* **1997**, *10*, 1285-1292; b) N. M. Dimitrijevic, P. V. Kamat and R. W. Fessenden, *J. Phys. Chem* **1993**, *97*, 615-618; c) M. Matusiak, S. Kadłubowski and P. Ulański, *Applied Sciences* **2021**, *11*, 10142; d) D. C. Grills, D. E. Polyansky and E. Fujita, *ChemSusChem* **2017**, *10*, 4359-4373.

[44] A. Migus, Y. Gauduel, J. L. Martin and A. Antonetti, *Phys. Rev. Lett.* **1987**, *58*, 1559-1562.

[45] a) S. Soldevila, M. Consuelo Cuquerella, V. Lhiaubet-Vallet, R. Edge and F. Bosca, *Free Radic Biol Med* **2014**, *67*, 417-425; b) K. Kobayashi, *Chem. Rev.* **2019**, *119*, 4413-4462; c) J. Ma, S. A. Denisov, A. Adhikary and M. Mostafavi, *Int J Mol Sci* **2019**, *20*; d) K. Kobayashi and S. Tagawa, *J. Am. Chem. Soc.* **2003**, *125*, 10213-10218; e) D. Schulte-Frohlinde, E. Bothe, G. Behrens and J. Opitz, *Journal of Radioanalytical and Nuclear Chemistry* **1986**, *101*, 209-220; f) S. V. Jovanovic, Y. Hara, S. Steenken and M. G. Simic, *J. Am. Chem. Soc.* **1995**, *117*, 9881-9888.

[46] N. A. Till, S. Oh, D. W. C. MacMillan and M. J. Bird, *J. Am. Chem. Soc.* **2021**, *143*, 9332-9337.

[47] Y. Kawamata, J. C. Vantourout, D. P. Hickey, P. Bai, L. Chen, Q. Hou, W. Qiao, K. Barman, M. A. Edwards, A. F. Garrido-Castro, J. N. deGruyter, H. Nakamura, K. Knouse, C. Qin, K. J. Clay, D. Bao, C. Li, J. T. Starr, C. Garcia-Irizarry, N. Sach, H. S. White, M. Neurock, S. D. Minteer and P. S. Baran, *J. Am. Chem. Soc.* **2019**, *141*, 6392-6402.

[48] J. F. Wishart, A. R. Cook and J. R. Miller, *Review of Scientific Instruments* **2004**, *75*, 4359-4366.

[49] M. Goez in *Chapter 3 Photo-CIDNP Spectroscopy*, *Vol. 66* Academic Press, **2009**, pp. 77-147.

[50] a) K. H. Mok and P. J. Hore, *Methods* **2004**, *34*, 75-87; b) J. Hore and R. W. Broadhurst, *Progress in Nuclear Magnetic Resonance Spectroscopy* **1993**, *25*, 345-402; c) M. Goez in *Elucidating Organic Reaction Mechanisms Using Photo-CIDNP Spectroscopy*, (Ed. L. T. Kuhn), Springer Berlin Heidelberg, Berlin, Heidelberg, **2013**, pp. 1-32; d) L. T. Kuhn in *Photo-CIDNP NMR Spectroscopy of Amino Acids and Proteins*, (Ed. L. T. Kuhn), Springer Berlin Heidelberg, Berlin, Heidelberg, **2013**, pp. 229-300; e) Y. Okuno and S. Cavagnero in *Photochemically Induced Dynamic Nuclear Polarization: Basic Principles and Applications*, pp. 283-314; f) R. Kaptein, *LJ Berliner and J. Reuben* **1982**, *5*.

[51] a) S. Perrier, E. Mugeniwabagara, A. Kirsch-De Mesmaeker, P. Hore and M. Luhmer, *J. Am. Chem. Soc.* **2009**, *131*, 12458-12465; b) L. Troian-Gautier, E. Mugeniwabagara, L. Fusaro, E. Cauët, A. Kirsch-De Mesmaeker and M. Luhmer, *J. Am. Chem. Soc.* **2017**, *139*, 14909-14912; c) L. Troian-Gautier, E. Mugeniwabagara, L. Fusaro, C. Moucheron, A. Kirsch-De Mesmaeker and M. Luhmer, *Inorg. Chem.* **2017**, *56*, 1794-1803.

[52] a) L. T. Kuhn, *Hyperpolarization methods in NMR spectroscopy* **2013**, 229-300; b) M. Goez, *Hyperpolarization Methods in NMR Spectroscopy* **2013**, 1-32; c) R. Kaptein in *Photo-CIDNP studies of proteins*, Springer, **1982**, pp. 145-191.

[53] a) E. Cauët, S. Bogatko, E. Mugeniwabagara, L. Fusaro, A. Kirsch-De Mesmaeker, M. Luhmer and N. Vaeck, *Inorg. Chem.* **2010**, *49*, 7826-7831; b) L. Troian-Gautier, E. Mugeniwabagara, L. Fusaro, C. Moucheron, A. Kirsch-De Mesmaeker and M. Luhmer, *Inorg. Chem.* **2017**, *56*, 1794-1803.

[54] J. R. B. John A. Weil in *Basic Principles of Paramagnetic Resonance*, **2006**, pp. 1-35.

[55] a) M. D. E. Forbes, L. E. Jarocha, S. Sim and V. F. Tarasov in *Chapter One - Time-Resolved Electron Paramagnetic Resonance Spectroscopy: History, Technique, and Application to Supramolecular and Macromolecular Chemistry*, *Vol. 47* Eds.: I. H. Williams and N. H. Williams), Academic Press, **2013**, pp. 1-83; b) C. Karunakaran and M. Balamurugan in *Chapter Five - Advances in Electron Paramagnetic Resonance*, (Ed. C. Karunakaran), Elsevier, **2018**, pp. 229-280.

[56] a) T. Maly, K. Zwicker, A. Cernescu, U. Brandt and T. F. Prisner, *Biochim. Biophys. Acta Bioenerg.* **2009**, *1787*, 584-592; b) D. Goldfarb, *Journal of Magnetic Resonance* **2019**, *306*, 102-108; c) D. Abdullin and O. Schiemann, *ChemPlusChem* **2020**, *85*, 353-372; d) T. Schmidt, J. Jeon, W.-M. Yau, C. D. Schwieters, R. Tycko and G. M. Clore, *Proc. Natl. Acad. Sci. USA* **2022**, *119*, e2122308119.

[57] T. Biskup, *Front. Chem.* **2019**, *7*.

[58] a) Y. Liu, B. Shi, Z. Liu, R. Gao, C. Huang, H. Alhumade, S. Wang, X. Qi and A. Lei, *J. Am. Chem. Soc.* **2021**, *143*, 20863-20872; b) T. Miura, R. Carmieli and M. R. Wasielewski, *J. Phys. Chem. A* **2010**, *114*, 5769-5778; c) T. Yago, Y. Kobori, K. Akiyama and S. Tero-Kubota, *J. Phys. Chem. B* **2002**, *106*, 10074-10081.

[59] X.-H. Liu, H.-Y. Yu, J.-Y. Huang, X.-T. Zhou, C. Xue and H.-B. Ji, *Chem. Commun.* **2023**, *59*, 243-246.

[60] a) R. C. S. Barbosa and P. M. Mendes, *Sensors* **2022**, *22*, 9541; b) S. Palzer, *Sensors* **2020**, *20*, 2745; c) A. B. E. Attia, G. Balasundaram, M. Moothanchery, U. S. Dinish, R. Bi, V. Ntziachristos and M. Olivo, *Photoacoustics* **2019**, *16*, 100144.

[61] A. G. Bell, *Am. J. Sci.* **1880**, *s3-20*.

[62] L. Lin and L. V. Wang, *Nature Reviews Clinical Oncology* **2022**, *19*, 365-384.

[63] A.-M. Bratu and C. Popa, *Journal of Optoelectronics and Advanced Materials* **2007**, *9*.

[64] a) M. Grzegorczyk, S. Pogorzelski and P. Rochowski, *J. Environ. Chem. Eng.* **2022**, *10*, 107983; b) R. H. Vafaie, R. S. Pour, A. Mohammadzadeh, J. H. Asad and A. Mosavi, *Photonics* **2022**, *9*, 526.

[65] a) W. Schindler, C. Haisch, H. A. Beck, R. Niessner, E. Jacob and D. Rothe, *SAE Transactions* **2004**, *113*, 483-490; b) F. Sgobba, A. Sampaolo, P. Patimisco, M. Giglio, G. Menduni, A. C. Ranieri, C. Hoelzl, H. Rossmadl, C. Brehm, V. Mackowiak, D. Assante, E. Ranieri and V. Spagnolo, *Photoacoustics* **2022**, *25*, 100318.

[66] L. Lin, X. Tong, P. Hu, M. Invernizzi, L. Lai and L. V. Wang, *Advanced Science* **2021**, *8*, 2003396.

[67] I. R. Gould, D. Ege, S. L. Mattes and S. Farid, *J. Am. Chem. Soc.* **1987**, *109*, 3794-3796.

[68] R. L. McCreery, *Raman spectroscopy for chemical analysis*, John Wiley & Sons, **2005**, p.

[69] a) A. Orlando, F. Franceschini, C. Muscas, S. Pidkova, M. Bartoli, M. Rovere and A. Tagliaferro, *Chemosensors* **2021**, *9*, 262; b) N. M. Ralbovsky and I. K. Lednev, *Chem. Soc. Rev.* **2020**, *49*, 7428-7453; c) Y. V. Kistenev, A. V. Borisov, A. A. Samarinova, S. Colón-Rodríguez and I. K. Lednev, *Sci. Rep.* **2023**, *13*, 5384; d) K. Bērziņš, S. J. Fraser-Miller and K. C. Gordon, *International Journal of Pharmaceutics* **2021**, *592*, 120034.

[70] S. E. J. Bell, *Analyst* **1996**, *121*, 107R-120R.

[71] A. Sabella, D. Spence and R. Mildren, *IEEE Journal of Quantum Electronics* **2015**, *51*, 1-1.

[72] a) H.-o. Hamaguchi and T. L. Gustafson, *Annu. Rev. Phys. Chem.* **1994**, *45*, 593-622; b) V. L. Piercy, K. H. Saeed, A. W. Prentice, G. Neri, C. Li, A. M. Gardner, Y. Bai, R. S. Sprick, I. V. Sazanovich and A. I. Cooper, *J. Phys. Chem. Lett.* **2021**, *12*, 10899-10905; c) Y. Hu, F. Zhan, Q. Wang, Y. Sun, C. Yu, X. Zhao, H. Wang, R. Long, G. Zhang and C. Gao, *J. Am. Chem. Soc.* **2020**, *142*, 5618-5626; d) M. Banno, K. Ohta, S. Yamaguchi, S. Hirai and K. Tominaga, *Acc. Chem. Res.* **2009**, *42*, 1259-1269; e) C. Turro, S. H. Bossmann, G. E. Leroi, J. K. Barton and N. J. Turro, *Inorg. Chem.* **1994**, *33*, 1344-1347.

[73] a) J. Kash, J. Tsang and J. Hvam, *Phys. Rev. Lett.* **1985**, *54*, 2151; b) H. Nagao, A. Matsuda, K. Nakamura and K. Kondo, *Appl. Phys. Lett* **2003**, *83*, 249-250; c) R. N. Dürr, P. Maltoni, H. Tian, B. Jousselme, L. Hammarstrom and T. Edvinsson, *ACS Nano* **2021**, *15*, 13504-13515.

[74] a) C. V. Arotsis and G. T. Babcock, *Methods in enzymology* **1993**, *226*, 409-431; b) G. Balakrishnan, C. L. Weeks, M. Ibrahim, A. V. Soldatova and T. G. Spiro, *Current opinion in structural biology* **2008**, *18*, 623-629; c) D. Buhrke and P. Hildebrandt, *Chem. Rev.* **2019**, *120*, 3577-3630.

[75] J. Ma, X. Zhang and D. L. Phillips, *Acc. Chem. Res.* **2019**, *52*, 726-737.

[76] D. Mitchell, M. Lukeman, D. Lehnherr and P. Wan, *Org. Lett.* **2005**, *7*, 3387-3389.

[77] a) J. M. Warman, G. H. Gelinck, J. J. Piet, J. W. Suykerbuyk, M. P. de Haas, B. M. Langeveld-Voss, R. A. Janssen, D.-H. Hwang, A. B. Holmes and M. Remmers, *Optical Probes of Conjugated Polymers* **1997**, pp. 142-149; b) S. A. Madbouly, A. A. Mansour and N. Y. Abdou, *European Polymer Journal* **2007**, *43*, 3933-3942; c) T. J. Savenije, A. J. Ferguson, N. Kopidakis and G. Rumbles, *J. Phys. Chem. C* **2013**, *117*, 24085-

24103; d) S. Kamba, J. Petzelt, E. Buixaderas, D. Haubrich, P. Vaněk, P. Kužel, I. Jawahar, M. Sebastian and P. Mohanan, *Journal of Applied Physics* **2001**, *89*, 3900-3906; e) A. Pashkin, P. Kužel, J. Petzelt, B. Gorshunov and M. Dressel, *Ferroelectrics* **2002**, *272*, 219-224.

[78] a) J. M. Warman, M. P. De Haas, J. W. Yerhoeven and M. N. Paddon‐Row, *Advances in Chemical Physics: Electron Transfer–from Isolated Molecules to Biomolecules. Part 1* **1999**, *106*, 571-601; b) M. Lindau and E. Neher, *Pflügers Archiv* **1988**, *411*, 137-146; c) A. McIntosh and F. Boucher, *Biophysical journal* **1991**, *60*, 1-7.

[79] I. Kosarev, V. Khorunzhenko, E. Mintoussov, P. Sagulenko, N. Popov and S. Starikovskaia, *Plasma Sources Science and Technology* **2012**, *21*, 045012.

[80] J. D. Earley, A. Zieleniewska, H. H. Ripberger, N. Y. Shin, M. S. Lazorski, Z. J. Mast, H. J. Sayre, J. K. McCusker, G. D. Scholes, R. R. Knowles, O. G. Reid and G. Rumbles, *Nature Chem.* **2022**, *14*, 746-753.

[81] E. P. Farney, S. J. Chapman, W. B. Swords, M. D. Torelli, R. J. Hamers and T. P. Yoon, *J. Am. Chem. Soc.* **2019**, *141*, 6385-6391.

[82] D. Uraguchi, Y. Kimura, F. Ueoka and T. Ooi, *J. Am. Chem. Soc.* **2020**, *142*, 19462-19467.

[83] a) S. L. Goldschmid, N. E. Soon Tay, C. L. Joe, B. C. Lainhart, T. C. Sherwood, E. M. Simmons, M. Sezen-Edmonds and T. Rovis, *J. Am. Chem. Soc.* **2022**, *144*, 22409-22415; b) B. D. Ravetz, N. E. S. Tay, C. L. Joe, M. Sezen-Edmonds, M. A. Schmidt, Y. Tan, J. M. Janey, M. D. Eastgate and T. Rovis, *ACS Cent. Sci.* **2020**, *6*, 2053-2059.

[84] S. Cerfontaine, S. A. M. Wehlin, B. Elias and L. Troian-Gautier, *J. Am. Chem. Soc.* **2020**, *142*, 5549-5555.

[85] F. Glaser and O. S. Wenger, *JACS Au* **2022**, *2*, 1488-1503.

[86] a) B. Pfund, D. M. Steffen, M. R. Schreier, M.-S. Bertrams, C. Ye, K. Börjesson, O. S. Wenger and C. Kerzig, *J. Am. Chem. Soc.* **2020**, *142*, 10468-10476; b) W. Zhao and F. N. Castellano, *J. Phys. Chem. A* **2006**, *110*, 11440-11445; c) M. Uji, T. J. B. Zähringer, C. Kerzig and N. Yanai, *Angew. Chem. Int. Ed.* **2023**, *62*, e202301506.

[87] a) J. K. White, R. H. Schmehl and C. Turro, *Inorg. Chim. Acta* **2017**, *454*, 7-20; b) S. Cerfontaine, L. Troian-Gautier, Q. Duez, J. Cornil, P. Gerbaux and B. Elias, *Inorg. Chem.* **2021**, *60*, 366-379; c) G. Li, M. D. Brady and G. J. Meyer, *J. Am. Chem. Soc.* **2018**, *140*, 5447-5456; d) A. Soupart, F. Alary, J.-L. Heully, P. I. P. Elliott and I. M. Dixon, *Inorg. Chem.* **2020**, *59*, 14679-14695.

[88] a) N. Body, R. Bevernaegie, C. Lefebvre, I. Jabin, S. Hermans, O. Riant and L. Troian-Gautier, *Chem-Eur. J.* **2023**, *n/a*, e202301212; b) P. Rana, B. Kaushik, K. Solanki, K. M. Saini and R. K. Sharma, *Chem. Commun.* **2022**, *58*, 11354-11377; c) C. H. Mak, X. Han, M. Du, J.-J. Kai, K. F. Tsang, G. Jia, K.-C. Cheng, H.-H. Shen and H.-Y. Hsu, *J. Mater. Chem. A* **2021**, *9*, 4454-4504; d) R. Hosseinzadeh, N. Aghili and M. Mavvaji, *Polyhedron* **2022**, *213*, 115631.

Entry for the Table of Contents

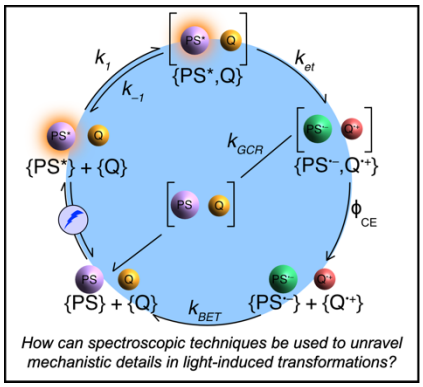

We describe several spectroscopic techniques available to determine key mechanistic processes in light-induced transformations and photoredox catalysis application. The reader is provided with a brief theoretical background as well as selected illustrative examples from the literature. The concept article ends with a personal perspective on the different avenues that will play a major impact in the future.

Institute and/or researcher Twitter usernames: @UCLouvain, @LudoTroian, @WELRI_asbl, @frsFNRS